Revista Mexicana de Astronomía y Astrofísica, **58**, 403–441 (2022)

https://doi.org/10.22201/ia.01851101p.2022.58.02.19

OBSERVATIONAL CONSTRAINTS ON THE HD 5980 WIND-WIND COLLISION

Gloria Koenigsberger[1], Nidia Morrell[2], D. John Hillier[3], Werner Schmutz[4], Roberto Gamen[5], Julia Inés Arias[6], Rodolfo Barbá[7], and Gabriel Ferrero[5]

Received May 5 2022; accepted August 18 2022

ABSTRACT

Analysis of spectral line profile variations observed over 6 decades in the Wolf-Rayet system HD 5980 lead to the conclusion that *Star A*, the variable member of the system, has always dominated the wind collision zone (WCZ), contrary to suggestions that before 1994 the stronger wind belonged to its close companion, *Star B*. The observed variations are caused by a combination of physical occultations, wind eclipses and emission and absorption originating in the WCZ. The effects caused by the leading WCZ branch, which folds around *Star B*, are clearly seen as it crosses our line of sight to *Star A* during the secondary eclipse. These effects can inform on the WCZ velocity and density structures. We speculate that differences in line profiles at the same orbital phase but at different epochs may be linked to changes in the WCZ radiative properties. The 2017-2020 spectra indicate that HD 5980 was in a higher activity state than during 2010-2015.

RESUMEN

Se presentan observaciones recientes del sistema múltiple HD 5980 ubicado en la Nube Menor de Magallanes que se complementan con los resultados de observaciones efectuadas desde los años 1950s. Encontramos que la componente *Star A*, que actualmente posee el espectro dominante tipo Wolf-Rayet, siempre ha sido la estrella con el viento más intenso. Las variaciones en los perfiles de líneas en emisión se explican con una combinación de los siguientes procesos: eclipses atmosféricos, emisión y absorción proveniente de la zona de interacción de los vientos, y ocultamiento de regiones de esta misma zona. Las observaciones de 2017-2020 indican un incremento en el nivel de actividad comparado con los años 2010-2015.

Key Words: binaries: eclipsing — stars: evolution — stars: mass-loss — stars: winds, outflows — stars: Wolf-Rayet

1. INTRODUCTION

The current understanding of the structure and evolution of massive stars is based on extensive theoretical models (Brott et al. 2011; Ekström et al. 2012; Heger et al. 2000; Maeder & Meynet 2000; Paxton et al. 2019), which, however, have many tunable parameters (e.g., mass loss rate, mixing length, among others). Constraints on these calculations and additional insights into the stellar structure are gleaned from theoretical atmosphere models from which synthetic spectra are produced and can then be compared with observations (Hillier & Miller 1998; Hillier & Lanz 2001; Puls et al. 2005; Hubeny & Lanz 1995). Through this comparison, fundamental stellar parameters are derived.

An underlying assumption in nearly all theoretical models is that the observed spectrum arises in a spherically symmetric atmosphere and wind. Thus, the spectra of binary systems are generally modeled

[1]Instituto de Ciencias Físicas, Universidad Nacional Autónoma de México, México.
[2]Las Campanas Observatory, The Carnegie Observatories, Chile.
[3]Department of Physics and Astronomy, & Pittsburgh Particle Physics, Astrophysics and Cosmology Center, University of Pittsburgh, USA.
[4]Physikalisch-Meteorologisches Observatorium Davos and World Radiation Center, Switzerland.
[5]Facultad de Ciencias Astronómicas y Geofísicas, Universidad Nacional de La Plata, and Instituto de Astrofísica de La Plata, CONICET–UNLP, Argentina.
[6]Departamento de Física, Universidad de La Serena, Chile.
[7]We mourn the loss of Rodolfo Barbá who passed away during the final preparation phases of this paper.

as the sum of the individual spectra arising in each of the two stars. However, massive stars emit intense ultraviolet radiation that drives a fast and dense stellar wind. If a binary system is composed of two massive stars, their mutual irradiation and wind interactions produce localized emission and absorption. Because an observer's line of sight to these localized line-emitting regions changes over the orbital cycle, their contribution to the observed spectrum produces orbital phase-dependent variations in the shape of spectral lines. This is referred to as line profile variability which, if significant, introduces uncertainties in the fundamental stellar parameters as derived from fitting spectra of single stars. Particularly noteworthy are the challenges involved in determining the contribution to the spectrum from a wind collision zone (WCZ).

The first observational evidence pointing to the presence of a WCZ in WN binary systems was obtained for V444 Cyg, HD 211853 and HD 90657 by Koenigsberger & Auer (1985). These authors detected orbital phase-dependent variations in the shape of the C IV λ1540 P Cygni, consistent with a WCZ dominated by the WR component of the system. Shore & Brown (1988) used higher spectral resolution UV data of V444 Cyg to reach a similar conclusion. Auer & Koenigsberger (1994) modeled the line profile variability in the N IV λ1718 line in V444 Cyg assuming it was due to wind eclipses, and found discrepancies between the model and the observations attributable to a WCZ. A similar analysis of the P V λ 1117 line observed in the FUV spectrum of HD 5980 led to the conclusion that the WR wind velocity structure is truncated on the hemisphere facing the companion due to the WCZ (Koenigsberger et al. 2006). These studies did not attempt to model the actual emission arising in the WCZ, an issue partially addressed by Luehrs (1997), who assumed that emission line sub-peaks in C III λ5696 observed in the WC7+O5-8 binary HD 152270 could be modeled as two separate emission lines originating in the outflowing WCZ streams. The same geometrical model has been applied to several other binary systems (Hill et al. 2000; Hill 2020; Hill et al. 2018) leading to the conclusion that the excess emission produced in the WCZ is responsible for between 10%-100% of the observed line emission, depending on the spectral line and the binary system. A somewhat different approach was employed by Flores et al. (2001) who analyzed the excess emission over that expected from an unperturbed, spherical wind in the V444 Cyg binary, concluding that the WCZ contributed no more than 12% of the total He II λ4686 line emission. The major deficiency in the simple models is that they rely on the assumption that superposed peaks on a line profile can be attributed uniquely to excess emission. This neglects the possible presence of superposed absorption that can cut into the broad underlying emission, resulting in an appearance that mimics the presence of emission peaks. In addition, in many cases there is no certainty that the underlying stellar wind line profile can be approximated with a stellar wind model line profile unless this profile is computed self-consistently with the perturbations introduced by the collision process.

The collision of two supersonic winds produces a double shock structure between them where radiation is emitted in wavelengths ranging from X-rays to the radio spectral regions (Corcoran 2003; Nazé & Rauw 2017; Pittard 2009; Pittard & Dawson 2018; Russell et al. 2016; Richardson et al. 2017; Lamberts et al. 2012). The shape of the collision region is determined primarily by the mass-loss rates and the wind velocities, and in its simplest representation, the shock region can be thought of as conical, and folded towards the star having the weaker wind momentum (Prilutskii & Usov 1976; Cantó et al. 1996). In reality, however, the geometry and physical conditions within the WCZ are significantly more complex, and require 3D numerical simulations to be understood. Complicating factors include the Coriolis effect which breaks the symmetry of the shock cone with respect to the line connecting the two stars, the UV radiation field from the stellar continua and from the WCZ itself which can alter the pre-shock wind structure, and the cooling efficiency of the shocked gas which determines the thickness and radiating properties of the shocked region. Simulations taking these factors into account show that binary systems having different combinations of wind, stellar and orbital parameters can result in a WCZ that is either a dominant contributor or a relatively minor perturbation (Pittard 2009; Russell et al. 2016; Richardson et al. 2017; Pittard & Dawson 2018). Thus, in a sample of massive binary systems, each binary may have a unique set of parameters, and these result in a WCZ whose emitting properties differ from those of any other binary. This makes it challenging to determine general properties that characterize the impact of a WCZ on the observed spectrum. It is equally challenging to ascertain the relevance of the WCZ on the emission line profiles and their variability.

The close binary system in HD 5980 provides what could be described as nearly laboratory conditions for studying wind-wind collision physics.

Specifically, it is a system in which the masses and orbital elements have remained constant during the more than 60 years over which it has been observed but in which one of the components has suffered significant luminosity and wind structure changes. HD 5980 is located in the periphery of the young stellar cluster NGC 346 in the Small Magellanic Cloud, and consists of two binary systems. The first of these displays a nitrogen sequence Wolf-Rayet (WN) type spectrum, indicative of chemical abundances corresponding to an advanced evolutionary state (Koenigsberger et al. 2014; Shenar et al. 2016; Hillier et al. 2019). Its two stars are massive ($\approx$60 $M_\odot$), luminous ($\approx 10^6$ $L_\odot$), and in a relatively close and eccentric orbit (P=19.3 d, $e = 0.3$). They are named *Star A* and *Star B*. The second binary system displays a late Of-type supergiant spectrum and is in a highly eccentric 97 d orbit with an unseen companion. This system, named *Star C*, contributed in 1978 approximately 40% of the light to the HD 5980 system (Perrier et al. 2009). There is at present no evidence indicating that both binary systems are gravitationally bound to each other. Hence, we focus hereafter on the *Star A* + *Star B* system.

Prior to its confirmation as a binary system, Smith (1968) and Walborn (1977) classified the observed WR spectrum as WN3, with the latter author remarking on the absence of N IV λ4058 in spectra of 1973 and 1977. Curiously, about a decade later Niemela (1988) detected this line, prompting her to propose WN3 and WN4 for *Star A* and *Star B*, respectively. Unknown at the time was that the system had initiated in $\approx$1980 a slow brightness increase and that all the WR emission lines, including λ4058, were becoming stronger. In 1993-1994, HD 5980 suffered two sudden and strong eruptive events, expelling $\approx 10^{-3}$ $M_\odot$ (Barbá et al. 1995; 1995ApJ...452L.107K). The absence of λ4058 in 1973 and 1977, its presence after that, and the appearance and strengthening of numerous UV Fe V and Fe VI lines leading up to the eruptions prompted Koenigsberger et al. (1995) to propose that the erupting component was the object responsible for the WR-type spectrum. At that time, however, it was believed that the dominant spectrum arose in *Star B*. However, subsequent RV measurements of these same Fe V/IV features showed them to instead follow the orbital motion of *Star A*, and Barbá et al. (1995) found indications of a large hydrogen abundance in the post-eruption spectra, not expected to be present in a *bona fide* WNE type star, as *Star B* was believed to be. Hence, the eruptive events were associated with an LBV-like process originating in *Star A* which, at the time, was believed to be an Of-type supergiant.

At the peak of the eruption, the dominant spectral type was WN11, as determined from spectra in the optical range (Heydari-Malayeri et al. 1997) or B1.5Ia$^+$ from UV spectra (Koenigsberger et al. 1996). After that, the brightness declined rapidly until $\approx$1996, remaining at an apparent plateau until $\approx$2002, after which it declined gradually. Currently, the N IV λ4058 emission is still significantly stronger than N V $\lambda\lambda$4603-21, indicating a WN6 spectral type. All strong lines follow the orbital motion of *Star A*.

Moffat et al. (1998) reviewed the behavior of HD 5980 prior to, during, and following the eruption and concluded that *Star A* must have been an O-type supergiant that through the eruptive process had transitioned to a WN star. They also proposed that the spectrum of this assumed O-type star and of *Star B* had been drowned out by wind collision emission, and proposed that the WCZ spectrum imitated that of a WN star. Applying the Luehrs method to spectra obtained in 1991/1992, they concluded that the WCZ extended perpendicular to the semimajor orbital axis and that the emission-line RVs could not be interpreted as representing in any way the orbital motion. This conclusion is in stark contrast with the CMFGEN radiative transfer model fit obtained to HD 5980's $\lambda\lambda$1200 -10000 spectral energy distribution and emission line intensities observed in 1999 and in 2014 (Koenigsberger et al. 2014; Shenar et al. 2016; Hillier et al. 2019). Thus, the bulk of the emission must arise in the stellar winds which, however, does not exclude the presence of additional emission and absorption arising in the WCZ.

The current scenario for HD 5980 is one in which *Star A* is a highly unstable hydrogen rich WN star and *Star B* is a hydrogen poor *bona fide* WN4 star, and that both objects have evolved quasi-homogeneously from $\approx$100 $M_\odot$ stars (Koenigsberger et al. 2014; Shenar et al. 2016; Hillier et al. 2019). This scenario, however, leaves open the important question as to why *Star A* is so unstable, a question that is highly relevant to understanding the late stages of the evolution of very massive stars. It also begs an explanation for the peculiar behavior of the N IV λ4058 line in 1973-1983 which would indicate that *Star B* was also somehow involved in the instability process.

In § 2 we describe the new data, summarize the historic data used in our analysis, and describe the measurements. In § 3 we present an overview of the system, including its known parameters, assumed ge-

ometry, and a definition of the orbital phases. In § 4 we present and discuss the radial velocity curves, the full width at half maximum variations in the emission lines and the hydrogen to helium line strength ratios. In § 5 we describe and discuss the line profile variability. The nature of *Star B* is discussed in § 6. § 7 contains a summary of the observational results and the conclusions.

2. OBSERVATIONAL MATERIAL

The new data presented in this paper were obtained at the Las Campanas observatories (LCO) with the Magellan Clay and Baade telescopes in 2007-2020 and with the DuPont telescope in 2015-2020. We also revisited all the previously analyzed spectroscopic data. The summary of spectra is listed in Table 1 where Column 1 gives the epoch in years of the observations, Column 2 the telescope or instrument, Column 3 the number of spectra available, Column 4 the type of dispersion (Low, Medium, High), Column 5 the approximate wavelength range covered, and Column 6 the reference where the spectra were first reported.

On the du Pont telescope, the standard setup was using the echelle spectrograph and a 1" slit. The spectral resolution of these data ranges from 0.15 to 0.22 Å (R ≈ 25000) and the wavelength coverage goes from 3500 to 8800 Å. Spectra were reduced with *IRAF*. The high resolution Clay (Magellan-II) spectra were obtained with the Magellan Inamori Kyocera Echelle spectrograph (MIKE) using a 0.7" slit and applying a 2×2 binning to both blue and red detectors. This configuration results in a spectral resolution of ≈34000 (FWHM ranging from 0.10 to 0.25 Å).

Reductions were carried out with a combination of specially designed IRAF scripts contained in the 'mtools' package developed by Jack Baldwin and available at Las Campanas website, and the usual 'echelle' tasks in IRAF.

The instrumental response in the echelle orders needs to be corrected in order to analyze line profile variability. In the case of very weak and narrow lines that lie in orders that are not densely packed with spectral lines, rectification of the echelle orders can be accomplished by fitting a function to the line-free continuum regions in the order. This method was applied to the echelle order containing N V λ4944, using a three to nine order spline function. This method, however, is useless for lines such as He II λ 5411 which occupy at least ≈64% of the echelle order, leaving available only very narrow continuum regions near the edge of the order for locating the continuum level. In addition, there is no guarantee that a function fit to the edges of an order will properly represent the continuum near the center. Although several of the LCO spectra were flux-calibrated using nearby standard stars, the continuum level near the edges of the orders generally departs significantly from the straight line expected over the ≈100 Å covered by the order.

The technique we have applied is to choose spectral lines for which adjoining orders are free from major line features and use these as representative of the response function. The best line to apply this technique is He II λ5411, which generally lies on order #35 in our LCO spectra, and for which the two adjoining orders (34 and 36) are feature-free. We thus normalized this He II line on all our du Pont-echelle spectra by dividing the counts registered in order #35 by the average counts of orders #34 and #36 for each pixel along the wavelength dispersion direction. This procedure yields a uniformly normalized set of line profiles. An additional advantage of using He II λ5411 is that there are no overlapping transitions from other abundant atomic species that contaminate it in the hot star spectra. Thus, it is a reliable line for probing the processes responsible for the line profile variability and for obtaining automated radial velocity and intensity measurements.

Foellmi et al. (2008) showed that the majority of the He II and He II+H emission lines in the HD 5980 spectrum undergo similar orbital-phase dependent variability. Inspection of our current spectra indicates that this is still the case, so the conclusions derived from the variability of He II λ5411 profiles are applicable to most other lines with the exception of N IV λ 4058. This line is in general narrower and the line profile variability is not as strong. Unfortunately, the echelle order on which it is found and the neighboring orders contain several other strong emission lines, making a reliable normalization in this region very uncertain.

Radial velocity and line strength measurements were performed using two methods. An automated procedure was used on the echelle orders that were uniformly normalized using neighboring orders. This procedure integrates over the emission line intensity above the normalized continuum level to obtain the total line strength and the intensity-weighted line centroid as defined in Koenigsberger & Schmutz (2020). This technique was applied to the He II λ 5411 line. Spectra for which a consistent continuum normalization from spectrum to spectrum is not straightforward were measured individually using the *IRAF* function that fits one or more Gaussians to a line profile, a method that provided the

TABLE 1

AVAILABLE SPECTROSCOPIC DATA

Epoch	Observatory/Instrument	Number	Disp	$\approx \Delta\lambda$ Å	Reference
1955-1965	SAO Radcliff	22	L	4000-4900	Koenigsberger et al. (2010)
1973	CTIO	1	L	3300-4800	N. Walborn (Priv. Comm.)
1977	CTIO	1	L	3400-4900	N. Walborn (Priv. Comm.)
1978	IUE	1	L	1150-2000	Moffat et al. (1989)
1979-1981	IUE	7	H	1150-2000	Moffat et al. (1989)
1979-1981	IUE	7	H L	1800-3250	Koenigsberger et al. (2010)
1986	IUE	12	L	1150-2000	Moffat et al. (1989)
1991-1992	IUE	10	H	1150-2000	Koenigsberger et al. (1994)
1993	BEFS ORFEUS	1	H	920-1180	Koenigsberger et al. (2006)
1994	CTIO IUE	1	L	1170-8000	Koenigsberger et al. (1998b)
1994-1995	IUE	18	H	1150-2000	Koenigsberger (2004)
1998-1999	ESO 2.1m FEROS	28	H	3900-8500	Schweickhardt (2000)
1999-2000	FUSE	2	H	920-1180	Koenigsberger et al. (2006)
1999-2000	HST STIS	6	H L	1200-10000	Koenigsberger et al. (2000)
2002	FUSE	8	H	920-1180	Koenigsberger et al. (2006)
2005-2006	ESO 2.1m FEROS	13	H	3700-9000	Foellmi et al. (2008)
2009-2010	LCO IMACS B&C MagE	6	L	optical	This paper
2009	HST STIS	1	H	1200-1700	Georgiev et al. (2011)
2006-2020	LCO du Pont echelle	52	H	3480-9500	This paper
2007-2019	LCO MIKE	8	H	3330-9150	This paper
2014, 2016	HST STIS	1	H L	1200-10000	Hillier et al. (2019)
2018-2020	LCO MagE	10	M	3000-9000	This paper

radial velocity measurements of N V λ4944 listed in Table 10. This line clearly splits into two components at orbital phases of maximum velocity and, because of its small transition probability, must be formed in high density regions such as near the continuum optical depth unity zone of the stellar wind. Hence, it is considered to be possibly the only emission in the optical spectral range that can be used to describe the binary orbital motion. Koenigsberger et al. (2014) measured it mostly on the non-echelle spectra to determine the orbital elements of *Star A* and *Star B*. Because this N V line is so narrow (GFWHM≈250 km/s in each star), there are available continuum segments on the echelle order on which it is located that can be used to normalize the spectrum. We have employed a spline function of 5th to 11th order (depending on the spectrum) which has produced a relatively flat continuum in the vicinity of this N V line, which was then measured by using two Gaussians to de-blend the velocity components. We also re-measured consistently the spectra reported in Koenigsberger et al. (2014), all of which were obtained prior to 2013.

The He II λ 4686 and He II+H β (Table 11), and the N IV λ 3483 and N IV λ 4058 (Table 12) lines in the FEROS, HST/STIS, and low-dispersion LCO spectra were also measured, but here using a single Gaussian fit. The corresponding tables list radial velocity (RV), equivalent width (EW), and full width at half maximum intensity (FWHM), and previously determined values listed in Koenigsberger et al. (2010).

A useful matrix of the observed spectra per orbital phase and epoch is given in Table 9, where one can see that a very good orbital phase coverage exists for Epochs 1998-1999 (FEROS) and 2010-2012 (du Pont echelle). In addition, several of the orbital phases obtained at LCO in 2017-2018 overlap with the earlier data allowing a same-phase, epoch-to-epoch comparison.

Unless noted otherwise, all of the line profiles and radial velocities that are discussed in the text of this paper are corrected for the +150 km/s SMC systemic velocity. This choice of systemic velocity is based on the heliocentric radial velocity +150 km/s that was obtained by Niemela et al. (1986) from the He II photospheric absorption lines of a sample of massive stars in NGC 346.

TABLE 2

HD 5980 PARAMETERS

Parameter	Value	Comment	Reference
P_{AB} [d]	19.2654	Orbital period *Star A* + *Star B*	Sterken & Breysacher (1997)
T_0 [HJD]	2443158.71	Initial epoch (periastron)	Sterken & Breysahcer (1997)
i [deg]	86(1)	Orbital inclination	Perrier et al. (2009)
e	0.314(5)	Orbital eccentricity (photometry)	Perrier et al. (2009)
e	0.297(35)	Orbital eccentricity (RV curves)	Kaufer et al. (2002)
e	0.27(2)	Orbital eccentricity (RV curves)	Koenigsberger et al. (2014)
ω_{per}[deg]	132.5(1.5)	Longitude of periastron (photometry)	Perrier et al. (2009)
ω_{per}[deg]	134(4)	Longitude of periastron (RV curves)	Koenigsberger et al. (2014)
a_A sini [$R_\odot$]	78(3)	*Star A* semimajor axis	Koenigsberger et al. (2014)
a_B sini [$R_\odot$]	73(3)	*Star B* semimajor axis	Koenigsberger et al. (2014)
a sini [$R_\odot$]	151(4)	Orbital semimajor axis	Koenigsberger et al. (2014)
$M_A \sin^3$i [$M_\odot$]	61(10)	*Star A* mass	Koenigsberger et al. (2014)
$M_B \sin^3$i [$M_\odot$]	66(10)	*Star B* mass	Koenigsberger et al. (2014)
r_{per} [$R_\odot$]	104	Periastron separation	Adopting e=0.314, a=151
r_{ap} [$R_\odot$]	199	Periastron separation	Adopting e=0.314, a=151
ρ_1	0.158(5)	Optically thick *Star A* relative radius	Perrier et al. (2009)
ρ_3	0.108(3)	Optically thick *Star B* " "	Perrier et al. (2009)
ρ_2	0.269(14)	Optically thick envelope " "	Perrier et al. (2009)
R_A [$R_\odot$]	24	*Star A* radius	From ρ_1 and a=151
R_B [$R_\odot$]	16	*Star B* radius	From ρ_2 and a=151
R_{env} [$R_\odot$]	41	*Star B* envelope radius	From ρ_3 and a=151
ℓ_A	0.398	Relative light contribution *Star A*	Perrier et al. (2009)
ℓ_B	0.300	Relative light contribution *Star B*	Perrier et al. (2009)
ℓ_C	0.302	Relative light contribution *Star C*	Perrier et al. (2009)
P_C [d]	96.56(1)	Orbital period *Star C*	Koenigsberger et al. (2014)
T_C [HJD]	2451183.40	Initial epoch *Star C* (periastron)	Koenigsberger et al. (2014)
e_C	0.815(20)	Orbital eccentricity *Star C*	Koenigsberger et al. (2014)
ω_{per}[deg]	252(3)	Longitude of periastron *Star C*	Koenigsberger et al. (2014)

3. OVERVIEW OF THE SYSTEM

Table 2 provides a summary of the HD 5980 parameters, with values that have been compiled from the references listed in the last column. Appendix A provides a detailed historical overview and describes the methods used to determine these parameters.

The eruptive variable in the system was named *Star A* by Barbá et al. (1996) and its close companion is *Star B*. This nomenclature has been retained ever since. *Star A* and *Star B* form an eclipsing system (Breysacher & Perrier 1980, 1991). The orbital phases throughout this paper are determined using the ephemerides of Sterken & Breysacher (1997): T_0=2443158.705, P=19.2654d, where T_0 corresponds to primary eclipse (*Star A* between the observer and *Star B*).[8]

Star A and *Star B* are in an eccentric orbit, and our adopted orbital configuration is illustrated in Figure 1 in a frame of reference with origin in *Star B*. Orbital phase ϕ=0 corresponds to the eclipse of *Star B* by *Star A*. The second eclipse occurs at ϕ=0.36 and periastron passage occurs at ϕ=0.061. The reason for choosing a frame of reference centered on *Star B* is that all the radial velocity (RV) measurements

[8]We have determined a possible revised ephemeris P_{Gamen}=19.2658d, T_{Gamen}=2443158.872, with the latter value being similar to that obtained by Foellmi et al. (2008), $T_{Foellmi}$=2443158.865. The difference in the phases as determined with the Sterken & Breysacher (1997) ephemerides and the revised one is <0.025, which has only a minor effect on the results of our current study. Hence, for consistency with our previous investigations, all our phases are calculated with the Sterken & Breysacher (1997) ephemeris.

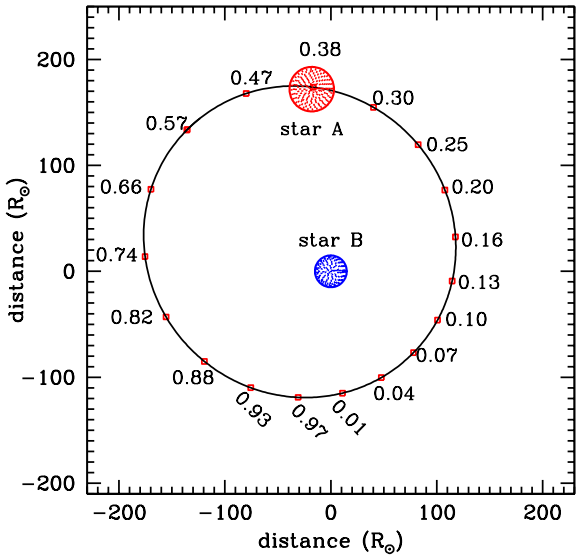

Fig. 1. *Star A* + *Star B* orbital phases in a coordinate system that is centered on *Star B* and an observer located at the bottom of the plot. Eclipses occur at ϕ=0 and 0.36, and periastron at ϕ=0.061, corresponding to ω_{per}=133° (Perrier et al. 2009). The relative radii are drawn to scale, using the values that were obtained by Perrier et al. (2009) and a semi-major axis of the elliptic orbit a=151 $R_\odot$ as derived by Koenigsberger et al. (2014). The color figure can be viewed online.

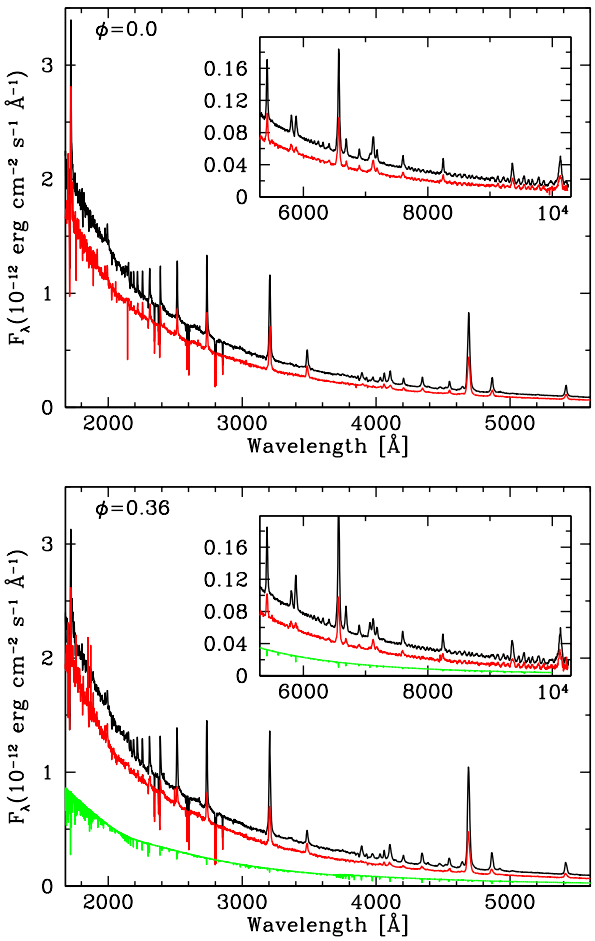

Fig. 2. Spectral energy distribution in epochs 1999-2000 (black) and 2014-2016 (red) obtained with *HST/STIS* showing the changes between the high (black) and low states (red) states. The top panel shows spectra at orbital phase ϕ=0 and the bottom panel at ϕ=0.36. The green spectrum in the bottom panel is a CMFGEN model of *Star C*. The color figure can be viewed online.

of the strong emission lines follow the expected orbital motion of *Star A*, except for a brief phase interval centered around orbital phase 0.36, which will be discussed below. The observer is located at the bottom so that the maximum approaching velocity of *Star A* occurs in the phase interval ≈0.66-0.82 and maximum receding velocity in the phase range ≈0.05-0.25. The relative sizes of *Star A* and *Star B* that are depicted correspond to the continuum emitting disk, R_A and R_B based on the results of Perrier et al. (2009) and Koenigsberger et al. (2014).

The spectral energy distribution (SED) of HD 5980 is extremely blue, as is evident in Figure 2, which illustrates the SED at both eclipses and at two different observation epochs separated by 15 years. The observed HD 5980 spectral energy distribution includes the continuum and the photospheric absorption lines from a "third light source", named *Star C*. This source was first discovered by Breysacher & Perrier (1980) and currently contributes approximately 30% of the total flux in the visual spectral region. Niemela (1988) showed that the photospheric absorptions remained static over the 19.3 d orbital period. Kaufer et al. (2002) discovered that these absorptions follow a highly eccentric ($e \approx 0.8$) orbit with a period P_C=97 d. This result was confirmed and refined by Koenigsberger et al. (2014), who also discussed the possible relation between the *Star A*+ *Star B* system and the *Star C* system. It is as yet not clear whether the two binary systems are bound and in a very long-period orbit, or whether it is a line-of-sight coincidence.

The photospheric absorption spectrum of *Star C* was analyzed by Georgiev et al. (2011) and Koenigsberger et al. (2002), and was shown to have a spectral type similar to that of an O5-7 supergiant. The CMFGEN model that was used in Hillier et al. (2019) to

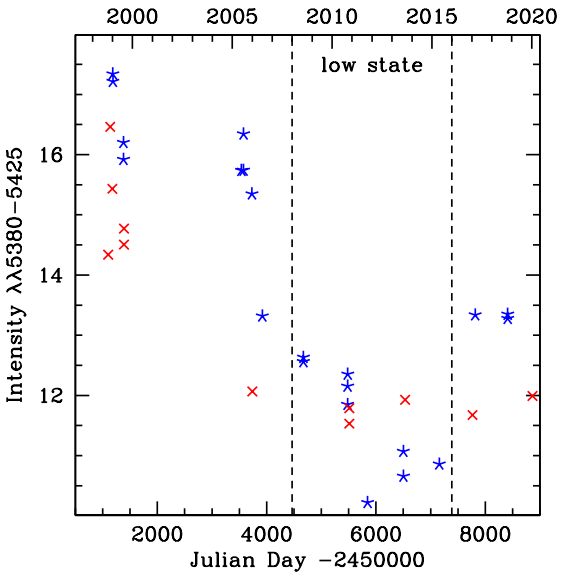

Fig. 3. Integrated intensity in the wavelength band $\lambda\lambda$5380-5440 in spectra obtained at elongation phases plotted as a function of Julian day. The corresponding epoch in years is listed in the top scale. Orbital phases ϕ=[0.15, 0.26] are plotted in red and [0.57, 0.80] are plotted in blue. The vertical lines mark the years 2008-2016 which enclose the time interval in which the system was in a low state. The color figure can be viewed online.

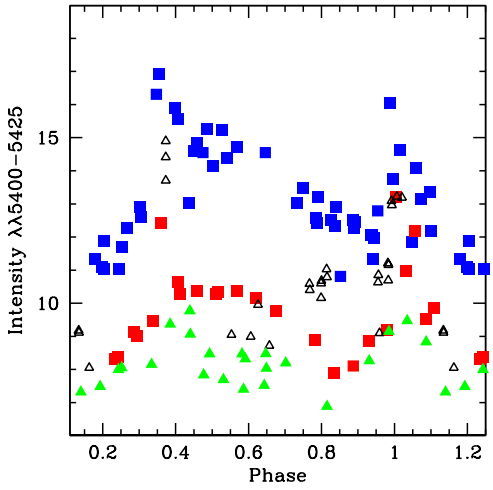

Fig. 4. Integrated intensity in the wavelength bands $\lambda\lambda$5400-5425 as a function of orbital phase. The epochs are: 1998-1999 (blue squares), 2005-2009 (black triangles), 2010-2015 (green triangles), 2017-2020 (red squares). The color figure can be viewed online.

model its SED is illustrated in the bottom panel of Figure 2. The full width at half maximum (FWHM) of *Star C*'s absorption lines is ≈75 km/s and thus easily identified when superposed on the WR emission lines. The secondary component that orbits the supergiant star has remained undetected, thus sparking the speculation that it may be a very rapidly rotating star whose photospheric absorptions are too broad and weak to be detected.

3.1. *The High and the Low Activity States*

The stellar wind properties of *Star A* changed significantly between the late 1990s and the current epoch. The most evident change is the diminution in emission line strength, as illustrated in Figure 3 where we plot the integrated intensity of He II λ5411 in the wavelength range $\lambda\lambda$5400-5425 in epochs 1998-2020. Plotted are only data at elongation phases, when eclipse effects are minimized. The "high" state following the 1994 outburst persists in 1998 and 1999, followed by a relatively rapid transition during ≈2005-2007 to a "low" state which persisted through ≈2010-2017. Light curves obtained during the transition and during the low state are illustrated in the appendix (Figure 24).

Also evident in Figure 3 is an increase in line intensity during 2017-2020, which suggests that the system was in a more active state. The orbital phase-dependent view of the same data is given in Figure 4, which indicates that in 2017-2020 maximum intensity is centered around orbital phase 0.5, very similar to the maximum observed during the high state. Conversely, Figure 4 also shows that during the low state of ≈2010-2015, there is a reduced line intensity after orbital phase ≈0.5, compared to other epochs. In this orbital phase interval the system is near apastron, and *Star A* is approaching the observer.

The high and low states can also be clearly identified in the HST/STIS spectra which provide the absolute-flux calibrated spectral energy distribution (SED) in the wavelength range $\lambda\lambda$1200-10000. Six orbital phases were obtained during the 1999-2000 high state. Unfortunately, only one spectrum at each eclipse during the low state could be acquired. Thus, we can only compare the SEDs for different epochs at eclipse phases. In the low state, both the continuum and the lines are weaker (Figure 2). The diminution in continuum flux at λ5470 is ≈27% and is approximately equal at both eclipses. The diminution in emission line flux (above the continuum level) is 20%-68% depending on the line, and differs considerably at primary eclipse compared to secondary eclipse (see Table 3).

TABLE 3

FLUXES AND VELOCITIES (IUE AND HST)

Epoch	Phase	$\langle F_c \rangle$	F_{5411}	F_{3483}	F_{4058}	V_{wind}
1999	0.83	1.26	2.20	2.39	1.35	1770:
1999	0.05	1.06	1.53	1.19	1.20	1380
1999	0.15	1.30	2.14	2.85	1.22	1350
1999	0.36	1.04	2.08	1.81	1.06	2500
1999	0.40	1.14	1.91	1.97	1.05	2100
2000	0.00	0.95	1.68	2.39	1.03	1500
2002	0.99	...	...	...	...	1860
2009	0.99	...	...	...	...	2260
2014	0.00	0.70	0.94	1.46	0.54	2110
2016	0.36	0.74	0.89	1.45	0.34	2800:

Notes: $\langle F_c \rangle$ is the average flux in the continuum in the wavelength band 5460-5480 Å given in units of 10^{-13} ergs/(cm^2 s Å). F_λ is the integrated flux over the emission line above the continuum level, given in units of 10^{-12} ergs/(cm^2 s). V_{wind} is an estimate of the wind velocity obtained from the edge of the He II λ1640 P Cygni profile given in km/s; values of 1999-2009 taken from Georgiev et al. (2011); the value of 1993 was measured on the PV 1117 Å line in the ORFEUS BEF spectrum that is reported in Koenigsberger et al. (2006).

4. RV CURVES, FWHM VARIATIONS AND H/HE LINE STRENGTHS

4.1. *RV Curves*

Figure 5 displays the RV measurements of N V λ4944 in the 2008-2020 spectra and the RV curves that correspond to the orbital solution given by Koenigsberger et al. (2014). This line arises from a transition between two excited states and requires a high density region, such as the base of a WR wind, in order to become visible in the spectrum. In a system with an orbital separation such as that of HD 5980, the inner wind region is unlikely to be subjected to perturbations caused by the radiation field of the companion or the wind-collision. Thus, Figure 5 clearly shows that there are two sources of N V λ4944 emission and leaves little doubt that the *Star A + Star B* system contains two very massive stars in an eccentric orbit, each of which has a wind dense enough to produce this emission.

Figure 5 includes the N IV λ4058 RVs that were measured on spectra of 1994-2020. Its phase-dependent behavior is very similar to that of the *Star A* RV measurements of N V λ4944, but with a smaller amplitude and larger scatter. N IV λ4058 is plotted once again in Figure 6 (top left) together with N IV λ3483, the latter showing a similar trend despite the scarcity of spectra containing this line.

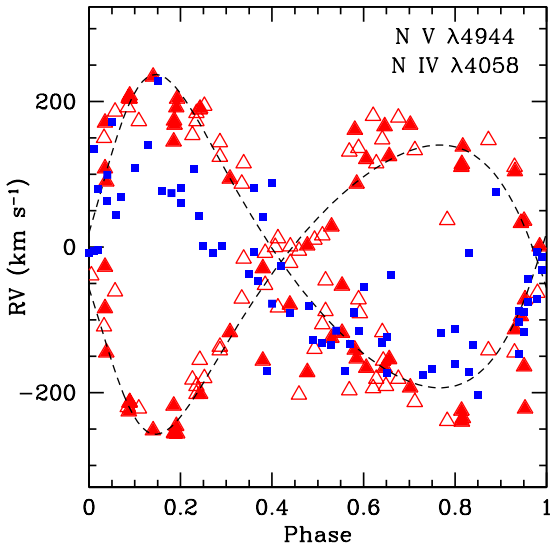

Fig. 5. Radial velocity of N V λ4944 as a function of orbital phase for epochs 2008-2012 (filled triangles) and 2013-2020 (open triangles), and N IV λ4058 (filled squares). The dash curves indicate the orbital solution given in Koenigsberger et al. (2014). The velocities are corrected for the SMC velocity. The color figure can be viewed online.

Figure 6 also shows the RV measurements of Hβ (top right) and He II λ4686 (bottom left) which have an even smaller variability amplitude than N IV λ4058.

The intensity-weighted RVs of He II λ5411 in the FEROS and du Pont echelle spectra are plotted in Figure 6 (bottom right). This type of measurement differs from that performed on the other lines (Gaussian fits) in that it is automated, does not depend on a chosen continuum level, and the wavelength range over which the centroid is computed remains fixed. Despite the different measuring method, the He II λ5411 RVs have a very similar behavior to those of Hβ and He II λ4686. Noteworthy in the He II lines as plotted in Figure 6 is the lack of negative RVs. The amplitudes and systemic velocities of the RV curves of WR stars can often depend on the line being measured. The differences are related to optical depth effects and the wind ionization and velocity structure. However, the RV curve amplitude of an emission line profile produced in a spherically symmetric, constant, wind should remain constant. In fact, even in the close WN6+O6 binary V444 Cyg (P_{orb}=4.2 d) the He II λ4686, λ5411, N IV λ4058 and N V $\lambda\lambda$ 4603-19 RV curves have very similar shapes and amplitudes (Münch 1950; Marchenko et al. 1994). Thus, the lack of nega-

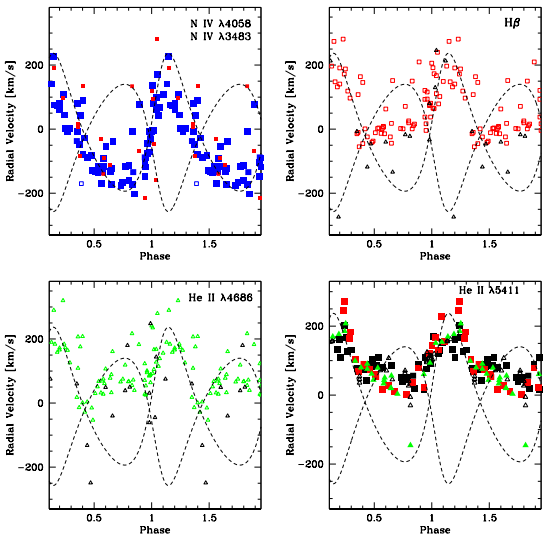

Fig. 6. Radial velocities of N IV λ4058 (top left, blue squares, Table 12), N IV$\lambda\lambda$3478-3484 (top left, red squares, Table 12, shifted by -80 km/s), Hβ (top right, red squares, Table 11), and He II λ4686 (bottom left, green triangles, Table 11). Black symbols correspond to historic values (Epochs 1955-1995). The bottom right panel shows the intensity weighted radial velocities of the He II λ5411 emission contained within the wavelength band $\lambda\lambda$5380-5440. The symbols correspond to: 1998-1999 (black squares), 2005-2009 (black triangles), 2010-2015 (green triangles), 2017-2020 (red squares). All RVs are corrected for the adopted +150 km/s SMC systemic velocity. The color figure can be viewed online.

tive RVs in the HD 5980 He II lines is a significant piece of information, and it leads to the conclusion that these lines arise in both stellar components, although *Star A* is in general the dominant contributor. This, of course, is not unexpected given the fact that the N V λ 4944 line indicates that both stars possess WR-type winds.

Foellmi et al. (2008) actually observed a resolved blue-shifted emission in N V λ4603 − 21, He II λ4341, Hγ and other lines at orbital phase ϕ=0.13. The excess blue emission in N IV λ4058 could also be inferred at ϕ=0.13, although it is not resolved. Hence, although *Star B* is clearly associated with WR-type emission lines, the dominant component is *Star A*. Furthermore, the fact that the He II RV curves have retained the same shape since the 1950s leads to the conclusion that *Star A* has been the dominant contributor to the emission line spectrum throughout all epochs at which it has been observed. Hence, it was a WR star when the 1993-1994 eruptions took place.

A second conclusion is that the intensity weighted centroids of He II λ5411 in epoch 2017-2020 have a larger positive velocity than other epochs at orbital phases when *Star A* is receding from the observer, indicating that something has recently changed in the system.

4.2. *Full Width at Half-Maximum (FWHM) Variations*

An outstanding feature of the HD 5980 emission lines is the high amplitude variation in the full width at half maximum which has been observed since the 1970s (for references, see the historic review in the Appendix). We measured the FWHM in He II λ4686 and Hβ in the majority of our new spectra and complemented these data with measurements of previous observations listed in Koenigsberger et al. (2010). The results, listed in Table 11 and summarized in Figure 7, can be described as follows. First, the variations are qualitatively the same in all epochs between 1955-2020, and they consist of two dips over the orbital cycle. The dips are centered ≈0.05 after eclipse minima, with the dip around primary minimum being significantly narrower than that at secondary minimum. Second, the descent in FWHM at primary minimum occurs very abruptly and is nearly identical in all observation epochs. The ascent after minimum appears to be similarly abrupt, but the data covering this part of the curve are insufficient to confirm this. Third, the maximum amplitude in 1955-1963 is very similar to that in 2005-2020 with max(FWHM)≈2000 km/s, contrasting with the 1998-2000 epoch in which max(FWHM)≈1650 km/s. This latter velocity is consistent with the derived wind velocity from UV P Cyg profiles in 1999-2000 at all orbital phases, except when *Star B* is in front (see Table 3). The downward shift of the FWHM curve of 1990-2000 reflects the fact that the lines were generally narrower during this post-outburst epoch, and it is consistent with the slower maximum wind speeds measured during those years.

The broader dip in the FWHM plot around the secondary eclipse is consistent with the presence of an extended envelope surrounding *Star B*, as has previously been found by Breysacher & Perrier (1980) and Perrier et al. (2009) from continuum light curves. Inspection of the Perrier et al. (2009) Figure 4 shows that the eclipse starts at ϕ ≈0.30 and ends at ϕ ≈0.42. As this is a continuum eclipse, the primary source of absorption/scattering of *Star A*'s continuum photons as they pass through *Star B*'s wind is electron scattering, which has a relatively small opacity. At spectral line frequencies, however, the opacity is much larger because the bound-bound transitions have cross-sections that are orders

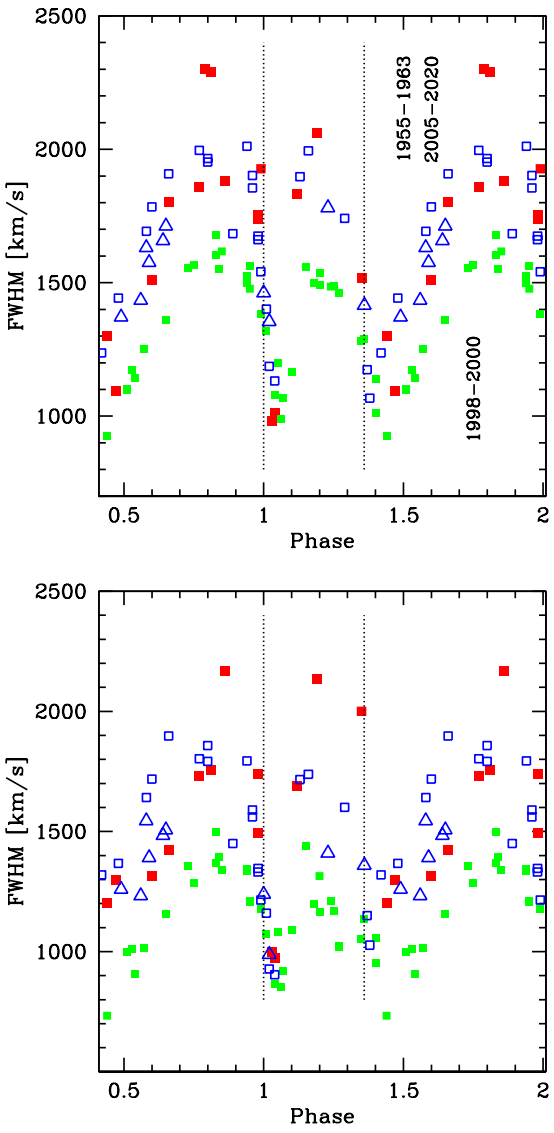

Fig. 7. Full-width at half maximum intensity of He II λ4686 (top) and Hβ (bottom) in epochs 1955-1965 (red), 1990-2000 (green), 2005-2013 (blue rectangles) and 2014-2020 (blue triangles). The color figure can be viewed online.

of magnitude larger than electron scattering. Hence, an occultation caused by wind material at spectral line frequencies takes up a larger fraction of the orbital cycle than the eclipse at continuum frequencies.

The continuum photons from a source that is passing on the far side of a spherically expanding wind are absorbed/scattered in the wind, and the projected velocity field is such that the resulting emission line profile is absorbed at all wavelengths, but given the opacity distribution, the effect is most prominent in the line wings (Auer & Koenigsberger 1994). This leads to a narrower emission line profile during the wind eclipse phases compared to the out-of eclipse phases.

Focusing now on the secondary dip in the FWHM plot, one can see that its descent initiates at $\phi \approx 0.3$ (similar to the continuum light curves) but the ascent does not end until $\phi \approx 0.6$. This leads to the conclusion that the envelope around *Star B* is more extended post-eclipse than pre-eclipse.[9] Hence, we interpret this asymmetry to be due to the trailing flow of the wind collision region which, as it passes in front of *Star A* , has a range of velocity components that provide added absorption to that of the intrinsic P Cyg absorption produced in *Star B*'s wind. An additional effect could be that *Star B*'s wind velocity is truncated by the collision with *Star A*'s wind, which would reduce the emission extent on the red side of the line center. Both effects taken together would naturally lead to a narrower emission feature.

We also measured the N IV λ4058 line (Table 12) and we find FWHM$\approx$750$\pm$100 km/s in epoch 1998-2000 and FWHM$\approx$850$\pm$100 km/s in 2005-2020 with no apparent orbital-phase variations. Koenigsberger et al. (2010) noted that this line underwent a factor $\approx$2 variations in the few spectra in which it was visible during 1955-1965. Given its sporadic appearance during the early epochs, the width variations in this line may have been associated with the WCZ alone.

4.3. *Hydrogen to Helium Line Strengths*

Foellmi et al. (2003) suggested that most of the WN stars in the SMC were likely to be WNha stars; i.e., a massive stars with a substantial amount of hydrogen in their outer layers and having wind properties intermediate between the Of stars and classical WN stars. The fact that CMFGEN models of *Star A* indicate that its wind contains large amounts of hydrogen is consistent with this idea.

We measured the flux and equivalent width in all the He II and He II+H lines in the HST/STIS spectra at three orbital phases in 1999, and in the HST/STIS observations of 2000, 2014 and 2016. These spectra were chosen for this purpose because they are uniformly flux-calibrated and they contain all He II and H I lines within the $\lambda\lambda$1200-10000 wavelength range. Each line equivalent width (EW) was normalized by the continuum flux at λ5000, as in Koenigsberger et al. (1998b). The results are illustrated in Figure 8. Lines containing H are systematically more intense than those without H, consistent with the

[9] Perrier et al. (2009) found evidence for a similar conclusion, though they considered the result marginal given the uncertainties in the light curve solution.

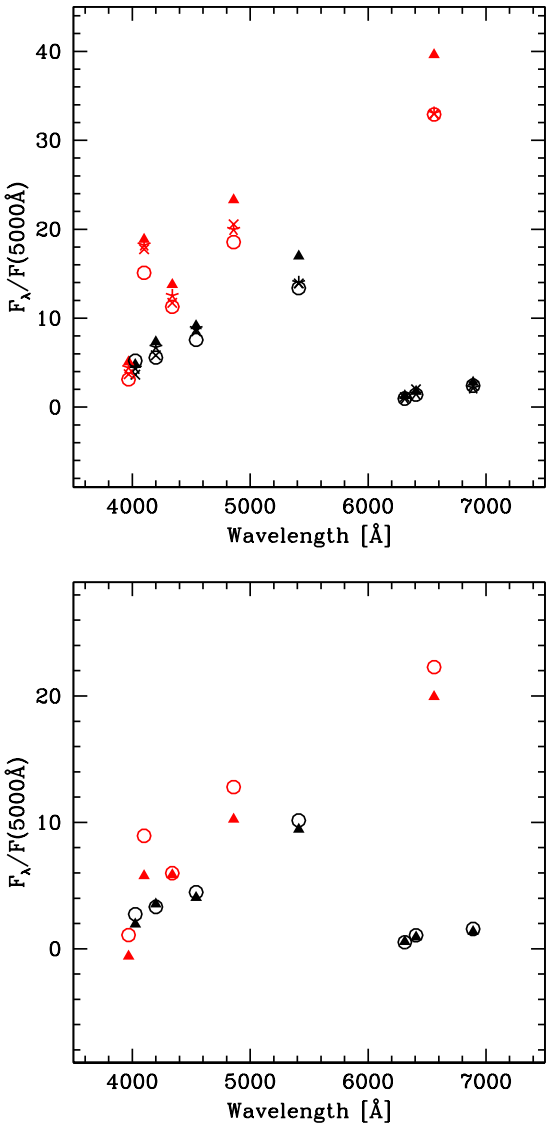

Fig. 8. Flux contained above the continuum level in lines of He II (black) and HeII+HI (red) in the STIS spectra normalized to the continuum flux at λ5000Å. *Top:* Spectra of 1999/2000 at orbital phases 0.15 (crosses), 0.83 (stars), 0.36 (triangles), 0.00 (circles). *Bottom:* Spectra of 2014 (circles), 2016 (triangles). The color figure can be viewed online.

finding that a significant amount of H is still present in the system. This is similar to the result found by Koenigsberger et al. (1998b) based on observations at a single orbital phase. Here, we can compare the results for several orbital phases. In particular, we find that in 1999-2000 the lines containing H at ϕ=0.36 (*Star B* in front) are stronger compared to ϕ=0 (*Star A* in front) while the reverse seems to occur in 2014-2016. One interpretation of this result is that the two components have different hydrogen mass fractions, which are reflected as they (partly) eclipse each other. However, the H/He ratios can also be affected by the conditions in the winds and the possible contribution coming from the WCZ, so at this stage we can only point out the phenomenon and await detailed modeling to arrive at an interpretation.

5. LINE PROFILE VARIATIONS AND WCZ SIGNATURES

The line profiles in HD 5980 are seldom found with the paraboloid shape predicted for a spherical wind. Its orbital phase-dependent line profile variability was amply discussed by Foellmi et al. (2008) and references therein. Moffat et al. (1989) attributed the UV variability to wind eclipses, and Moffat et al. (1998) and Breysacher & François (2000) discussed the optical lines from a qualitative standpoint, concluding that the line profile variations were dominated by the WCZ emission. However, the variations have never been systematized in the context of the epoch-to-epoch variability of *Star A*'s wind.

The emission produced in the WCZ is only one of the factors governing the line profile variability. The other factors are wind eclipses, physical occultation of wind and WCZ emission, lack of emission due to the "hole" in *Star A*'s wind which is filled with *Star B*'s wind, and absorption along the line of sight arising in the WCZ. The wind eclipses cause an emission line to become narrower and weaker due to absorption by the wind that is flowing both toward and away from the observer (Koenigsberger & Auer 1985; Auer & Koenigsberger 1994). The absorption along the line of sight arising in the WCZ acts in a similar manner, but its velocity field is very different. The asymmetrical configuration of the WCZ and the possibility that it is radiative, added to the other processes that affect the line profiles, require at least a 2D radiative transfer calculation in order to fully understand the line profiles and extract the information which they encode. A first step, however, is to constrain the importance of the non-spherically symmetric contribution in shaping the emission lines.

The focus of this paper is to identify the contribution from the WCZ, for which we will use Figure 9 in order to guide the ideas. This figure is an artistic representation of the WCZ and the assumed wind of *Star B* that is contained within it. It is based on the following considerations. The wind momentum ratio in HD 5980 is given by $\eta=\dot{M}_B V_B/\dot{M}_A V_A$, where $\dot{M}_B$ and $\dot{M}_A$ are the mass-loss rates of *Star B*

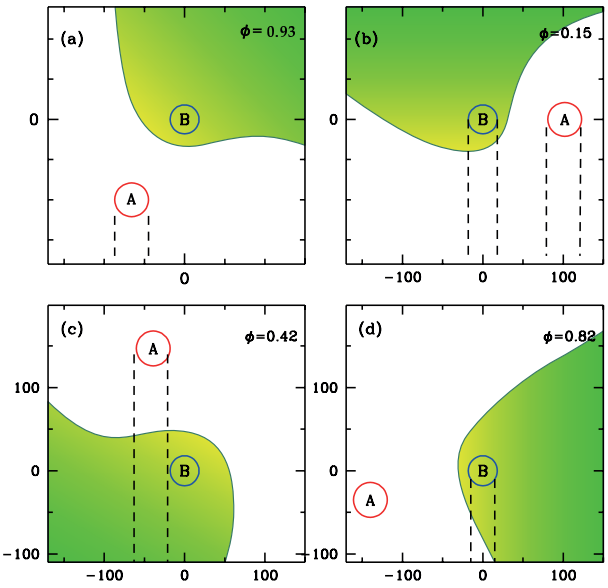

Fig. 9. Schematic illustration showing some of the sightlines (dash lines) through the wind of *Star A* and the one crossing *Star B* + WCZ (green). The assumed hottest shocked regions are yellow-colored. The circles correspond to the continuum-emitting radii of both stars as determined by Perrier et al. (2009) and are drawn to scale with respect to the orbital separation, which is given in $R_\odot$ in the axes. *Star B* is drawn at the origin of the coordinate system. Each panel represents a different orbital phase as indicated. The observer is at the bottom of the figure. The color figure can be viewed online.

and *Star A* respectively, and V_B and V_A are the corresponding wind velocities where the winds collide. The values of *Star A*'s velocities and of $\dot{M}_A/\sqrt{(f)}$ are available for the years 2000, 2002 and 2009 from Georgiev et al. (2011) and for 2014 from Hillier et al. (2019). The parameter $\sqrt{(f)}$ is the wind filling factor. The wind of *Star B* is assumed to correspond to that of a WNE star and to remain fairly stable from epoch to epoch. The derived values of η for epochs 2000-2014 are listed in Table 4, and lie in the range 0.13-0.16, confirming that the contact discontinuity of the shocks folds around *Star B*. Additionally, the WCZ is skewed with respect to the line connecting the centers of the two stars due to the Coriolis effect, which introduces an asymmetry between the leading and the trailing shocks (Gayley 2009; Lamberts et al. 2012).

A more precise shape of the WCZ requires calculations that are beyond the scope of this paper. For example, the shock-heated gas is contained between two shocks located on either side of the CD. Pittard & Dawson (2018) find that adiabatic shocks

TABLE 4

WIND MOMENTUM RATIO[a]

Epoch	$\dot{M}_A/\sqrt{(f)}$	V_A	f	η
Year	$10^{-4}\mathrm{M}_\odot\mathrm{yr}^{-1}$	$\mathrm{km\,s}^{-1}$	...	...
2000	3.5	2000	0.025	0.13
2002	2.5	2200	0.025	0.16
2009	2.3	2440	0.025	0.16
2014	1.4	2100	0.010	0.15

[a]Assuming *Star B* has a constant wind, $\dot{M}_B = 2\times10^{-5}\,M_\odot\,\mathrm{yr}^{-1}$, $V_B = 2200\,\mathrm{km/s}$, $f = 0.1$.

flare beyond the CD in both the primary and secondary winds by ≈20 deg. The CD opening angle of an adiabatic collision can be estimated using the expression given by Gayley (2009) with the modification of Pittard & Dawson (2018): θ=2 $\tan^{-1}(\eta^{1/3})$. This yields $\theta_{CD} \approx 54$ deg and it then follows that θ_2 ≈34 deg (*Star B*'s shocked wind) and θ_1 ≈74 deg (*Star A*'s shocked wind). However, Pittard & Dawson (2018) note that the shocks in HD 5980 are most likely to be highly radiative and thus the above approximations may not be valid. Also, the skew angle depends on the orbital motion which, in an eccentric binary such as HD 5980, varies over the orbital cycle, and the wind speed which may be affected in the vicinity of the shock by radiative braking (Gayley et al. 1997). Finally, the wind properties of *Star B* have only been inferred from the notion that it is a WN4 type star but are not known for certain, and this introduces a major uncertainty into any WCZ calculation.

5.1. *The Same Profiles are Observed at the Same Phase in Different Epochs*

Given the unstable properties of HD 5980, it is somewhat surprising to find that emission-line profiles obtained at the same orbital phase in different epochs are nearly identical. This is illustrated in Figure 10 where we plot He II λ5411 in the phase bins centered on $\phi \approx 0.24$ and 0.60. The left panels show that for $\phi \approx 0.24$ the spectra of 2010 and 2013 are nearly identical and they are very similar to the ones observed in 2017 - 2020. The right panels show that for $\phi \approx 0.6$, the profiles of 2010 and 2013 are also nearly identical. The more recent spectra (2017-2020), however, differ considerably from those of the earlier epochs in the same phase bin. Specifically, the broad blue-shifted absorption located near line center that is present in the earlier epochs is now replaced by emission, and the line intensity relative to the continuum is stronger. This is consistent with

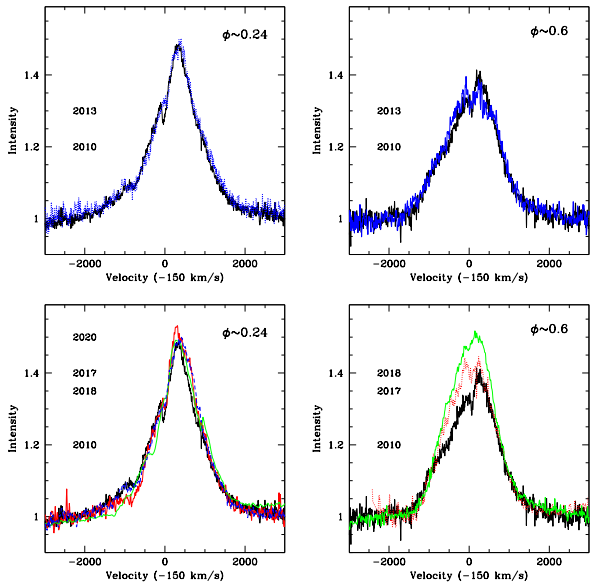

Fig. 10. Left: Line profiles of He II λ5411 in the orbital phase bin 0.24-0.25 in spectra of 2010 (black, top and bottom), 2013 (blue, top), 2017 (red, bottom), 2018 (green, bottom), 2020 (blue dashes, bottom) showing a nearly identical shape. Right: The same line in the phase bin 0.58-0.64 in spectra of 2010 (black, top and bottom), 2013 (blue, top), 2017 (red, bottom) and 2018 (green, bottom) showing a significant change in the 2017 and 2018 profiles compared to 2010-2013. The narrow absorption near line center belongs to the photospheric spectrum of *Star C*. The color figure can be viewed online.

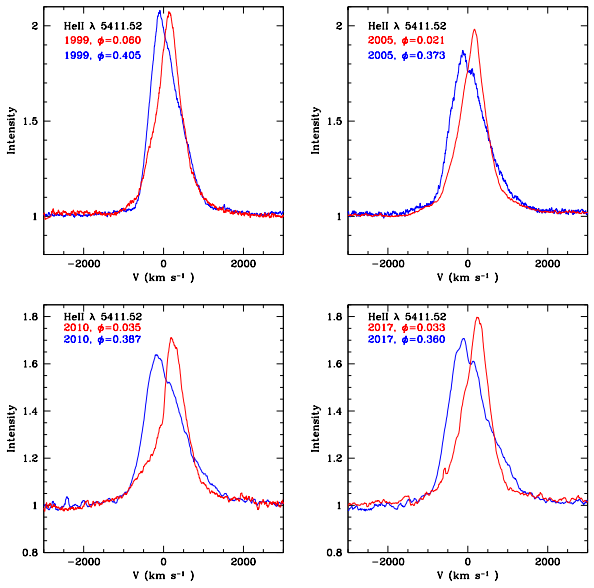

Fig. 11. Line profiles of He II λ5411 at post-primary eclipse (red, ϕ >0, *Star A* in front) and post-secondary eclipse (blue, ϕ >0.36, *Star B* in front). Each panel corresponds to a different epoch. The general behavior has remained the same over the time frame 1999-2017. The color figure can be viewed online.

the differences already noted for this orbital phase in Figure 4.

Inspection of Figure 9 and Figure 1 suggests that the culprit for the absorption during the low state (2010 and 2013) is likely to be the trailing WCZ wake which at the ϕ ≈0.6 orbital phase is in the foreground of both *Star A* and *Star B*. The absence of this absorption in 2017-2018 may be due to significantly stronger emission in the trailing wake which drowns out the absorption, or a reduced optical depth along the line of sight to the background continuum sources. A similar inspection applied to the ϕ ≈0.24 bin discloses that the only material in the sightline to *Star A* is its own wind. The change in the line profile between 2010 and 2020 is minimal. It is surprising that such a minimal difference in line profiles at ϕ=0.24 (which imply only a small change in wind structure) could have such a large effect on what is observed at ϕ ≈0.6. Thus, if our interpretation is correct, it seems like only a small change in *Star A*'s wind is necessary to noticeably alter the WCZ emitting properties.

A broad blue shifted absorption that is superposed on HD 5980's emission lines near line center is a feature that frequently appears. An example can be seen Figure 10. Often, a similar feature is observed on the red side of line center. In both cases, its total width is of the order of 500 km/s and its centroid can be displaced by as much as 1000 km/s from line center which precludes it from being a photospheric absorption. One possible explanation is that it originates at the base of one of the winds, where the initial acceleration takes place. However, this would not explain it when it is red-shifted. Thus, another possible explanation is an eclipse effect, when emitting material that is flowing away from us is occulted (that is, there is missing light within a particular velocity range). Inspection of Figure 9 shows in the top left panel an orbital phase at which *Star A* would block a fraction of the emission from the receding WCZ, and the bottom right panel shows a phase at which *Star B* would block a fraction of this light.

5.2. *Asymmetric Outflow at Conjunctions*

We now turn our attention to the line profiles around the conjunction phases. Figure 11 shows the line profiles obtained within 0.05 in phase after the ϕ=0.36 eclipse in four epochs between 1998 and 2017. These profiles are compared to those obtained

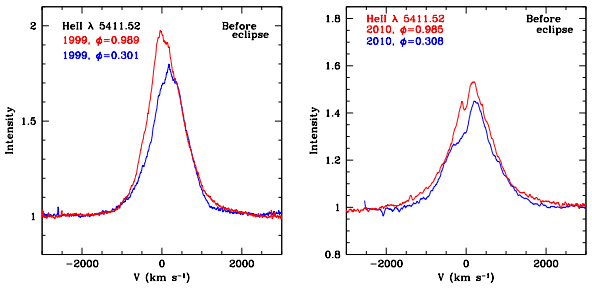

Fig. 12. Line profiles of He II λ5411 at phases just before each eclipse (ϕ=0.99, red, and ϕ=0.30, blue) in epoch 1999 (left) and epoch 2010 (right). The color figure can be viewed online.

right after the opposite eclipse (ϕ=0) and clearly indicate that a significant fraction of the He II λ5411 emission arises in material that is flowing toward us when *Star B* is in front. The profiles when *Star A* is in front are redshifted, but this is likely due to a combination of the above-mentioned outflow, which at this phase is moving away from us, and the wind eclipse due to *Star A*'s wind which lies along the sightline to *Star B*. The relative shift between the maxima in each pair of orbital phases is 229 km/s in 1999, 281 km/s in 2005, 385 km/s in 2010, and 377 km/s in 2017. These epoch-to-epoch variations correlate with the increasing wind speed recorded for *Star A* based on the UV P Cyg absorption components. They also correlate with the relative intensity of the two maxima at each epoch. Thus, the qualitative nature of the profile variations is the same in all epochs: the line profile is always blue-shifted at $\phi \approx$0.36.

Figure 12 compares the line profiles obtained at orbital phases just before eclipses, ϕ=0.301-0.305 (*Star B* in front) and ϕ=0.985-0.989 (*Star A* in front) for Epochs 1998-1999 and 2010-2012, the only two epochs for which we have such similar orbital phases. Once again, the most important point to note is that, despite the significant difference in line strengths between the high and the low states, the qualitative nature of the variation is the same. Also noteworthy is that the profiles just prior to $\phi \approx$0.36 do not show the prominent blue-shifted emission seen after ϕ=0.36 but instead have a strong absorption. This now brings us to the role of the leading branch of the WCZ.

5.3. *The WCZ Leading Branch*

The properties of the WCZ are determined by the velocity of the winds when they collide. The skewed WCZ orientation with respect to the line connecting the centers of the two stars introduces an asymmetry between the leading and the trailing shocks. In the case of an unequal wind momentum ratio, as in HD 5980, Pittard (2009) finds that the emission measure of the WCZ is dominated by the shocked gas of the weaker wind, most of which is in the leading arm. Hence, the relative location of the leading WCZ arm with respect to our sightline to *Star A* and *Star B* will determine whether this shocked gas signals its presence as an absorption in the line profile or as an emission. Upon inspection of Figures 9 and 10 we see that right before ϕ=0.36 the leading arm lies directly between us and *Star A* and it is flowing almost directly toward us[10]. Hence, its presence should be evident as blue-shifted absorption. After the ϕ=0.36 conjunction, the leading branch is still flowing toward us but it is no longer projected onto *Star A* and hence we should observe it in emission. This behavior is precisely what is observed.

A detailed look at the transition that occurs as the leading WCZ arm passes in front of *Star A* around ϕ=0.36 is shown in Figure 13, which illustrates two pairs of profiles obtained in the same orbital cycle. These pairs of profiles show that just prior to eclipse (ϕ=0.31-0.33) there is a prominent blue absorption that "eats into" the underlying emission, while just after eclipse (ϕ=0.39) this absorption is replaced by emission. The two pairs of profiles correspond to the two epochs, 2010 and 2013. The absorption in 2010 extends from near line center to approximately $-$800 km/s, which provides a constraint on the flow velocity of the leading arm in that portion projected onto *Star A*.

A similar result is found when comparing the pre- and post-eclipse line profiles of 1999, 2017 and 2018 shown in Figure 14. However, in this case the only available post-eclipse spectra are at phases $\approx$0.41 and pre-eclipse phases $\approx$0.22-0.30. The latter display a different behavior near the base of the line. Specifically, they show the presence of emitting material flowing toward us with projected velocities $>$ 1000 km/s, compared to the post-eclipse profiles which appear more absorbed. This fast emission (compared to the profiles closer to eclipse) is also seen in the earlier epochs as illustrated in Figure 15 where we compare the profiles shown in Figure 13 with profiles obtained further from central eclipse.

5.4. *Line Profiles at Elongations*

At elongation phases, the sightline to the close vicinity of *Star A* intersects only *Star A* wind, while the sightline to *Star B* intersects its wind and the

[10]See also the geometry in Figure 2 in Lamberts et al. (2012) and Figure 9 of Parking & Pittard (2008).

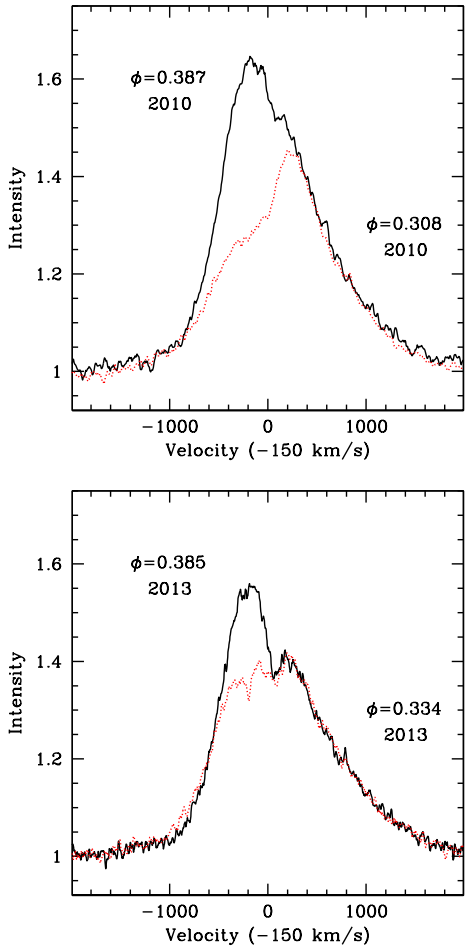

Fig. 13. Spectra pre- and post-secondary eclipse for epochs 2010 (left) and 2013 (right) illustrating the absorption caused by the WCZ leading branch as it first passes in front of *Star A* (red profiles) and the emission that appears shortly thereafter when it is no longer projected onto the *Star A* bright background continuum. The color figure can be viewed online.

WCZ (which includes shock-heated *Star A* and *Star B* wind). Depending on the aberration angle, some of the WCZ material may be flowing away from the observer, while some is flowing perpendicular to the sightline and other portions have velocity components toward the observer. Of all this material, that which lies along the sightline to the *Star A* and *Star B* cores can produce absorption.

Illustrated in Figure 16 is the profile of He II λ1640 at the two elongation phases observed in 1999, $\phi \approx 0.8$ (*Star A* approaching the observer) and $\phi \approx 0.1$-0.2 (*Star A* receding). These profiles are shifted in velocity space to correct for *Star A*'s orbital motion, so any excess in the line profile can

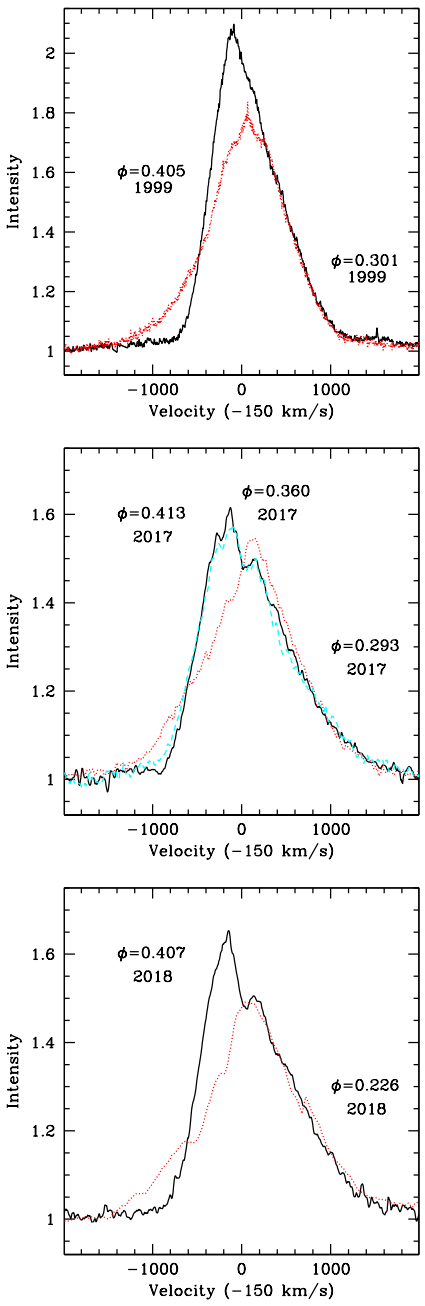

Fig. 14. Spectra pre- and post-secondary eclipse for epochs 1999 (top), 2017 (middle) and 2018 (bottom) illustrating the absorption caused by the WCZ leading branch as it first passes in front of *Star A* (red profiles) and the emission that appears shortly thereafter when it is no longer projected onto the *Star A* bright background continuum. The middle panel shows the line profile during eclipse (magenta) which is nearly identical to the post-eclipse profile. Spectra are shifted in the velocity scale to correct for the orbital motion of *Star A*. The color figure can be viewed online.

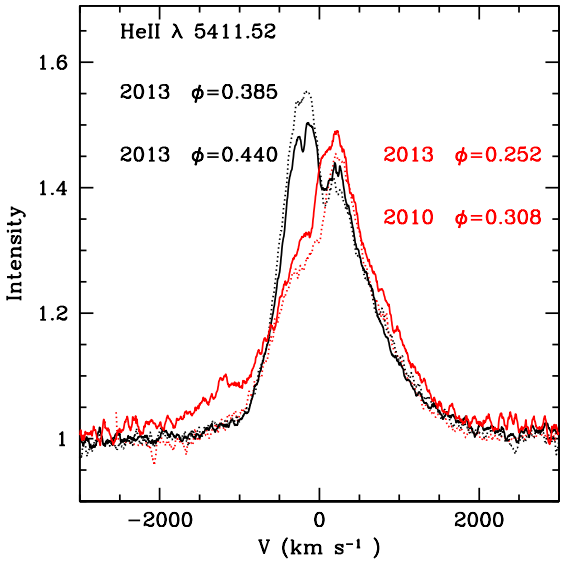

Fig. 15. Spectra pre- and post-secondary eclipse showing that the physical eclipse of the two stars plays little or no role in producing the variability around ϕ=0.36, but rather it is associated with the WCZ geometry. Epochs 2010 and 2013 are both in the low state. The color figure can be viewed online.

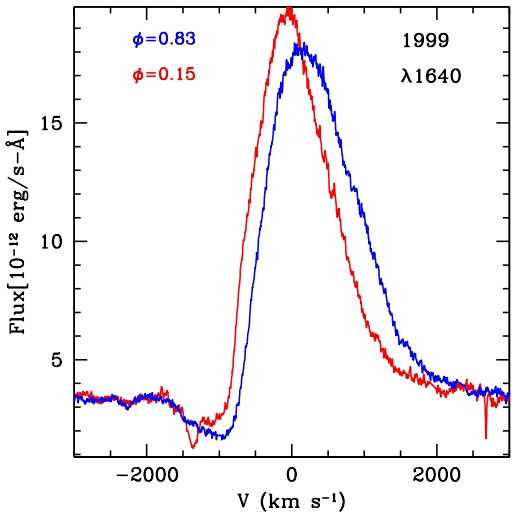

Fig. 16. Line profiles of He II λ1640 obtained in 1999 at elongations in the rest frame of *Star A*. The color figure can be viewed online.

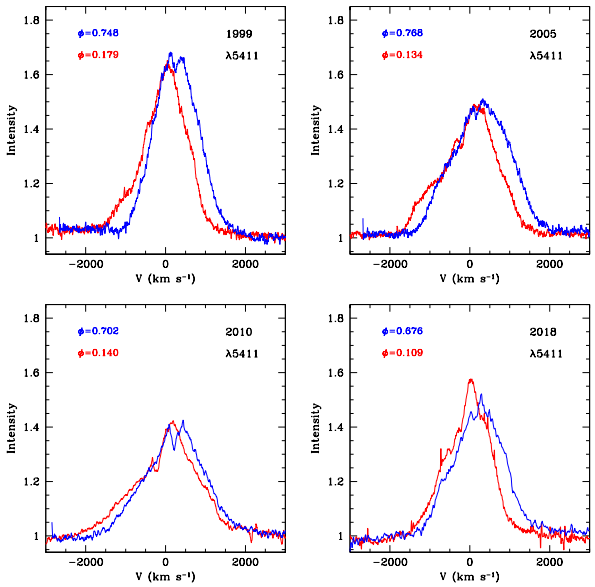

Fig. 17. Line profiles of He II λ5411 at elongations in the rest frame of *Star A*. Top: Epochs 1999 (left) and 2005 (right). Bottom: 2010 (left) and 2018 (right). The color figure can be viewed online.

be associated with emission arising in *Star B* and/or the WCZ. There is indeed such an excess redward of line center at $\phi \approx$0.7, which is consistent with an origin in or near *Star B*. This excess emission shows up blueward of line center and around line center at the opposite elongation, when *Star B* is approaching the observer, and it fills in a part of the intrinsic *Star A* P Cygni absorption.

Analogous pairs of profiles for He II λ5411 are shown in Figure 17 for epochs 1999, 2005, 2010 and 2018. The same excess red emission at $\phi \approx$0.7 is evident in each epoch, but the blue excess at the opposite phase is concentrated at higher expansion speeds, i.e., closer to the base of the broad emission. This is probably only a consequence of the smaller optical depth in He II λ5411 compared to He II λ1640. Interestingly, the pairs of of He II λ5411 profiles show that the amount of excess red-shifted emission scales with the overall line intensity. The smallest amount of excess emission is seen in the 2010 spectra, when line intensities were near their minimum and the system was in the low state.

Georgiev et al. (2011) showed that increasing line emission correlates with increasing visual magnitude and, at the same time, correlates with decreasing wind velocity. If we assume that a smaller *Star A* wind speed implies that its density is higher, this would mean that the WCZ is being fed with a higher density wind at epochs other than 2010, which would result in a larger emission measure. Following this line of reasoning leads to the conclusion that the excess emission along the line wings of the He II lines originates in the WCZ, and that this shocked region lies in the close vicinity of *Star B*.

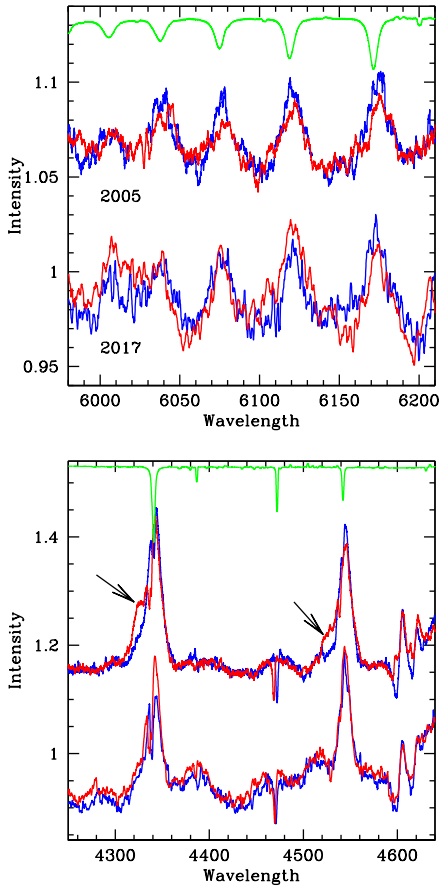

Fig. 18. Line profiles of He II and other lines obtained in 2005 at ϕ=0.98 (blue) and 0.13 (red) compared to those of 2017 at ϕ=0.98 (blue) and 0.08 (red). Spectra are shifted in wavelength to correct for *Star A* orbital motion. The 2005 spectra are shifted vertically for clarity. The arrows point to the blue-shifted excess emission at ϕ=0.08 in 2005 and absent in 2017. The green curve shows the predicted *Star C* photospheric absorption spectrum. The color figure can be viewed online.

The *HST/STIS* 2016 observation of HD 5980 (ϕ=0.36) revealed a very peculiar shape of the C IV λ1550 P Cygni profile: there was notable excess emission blueward of line center extending out to approximately −900 km/s with respect to the HD 5980 rest frame. Because this C IV doublet is a resonance line, any outflowing material lying along the line of sight to either *Star A* or *Star B* would appear in absorption, not emission. Given the above discussion and our conclusions from the optical observations, the C IV excess emission must also arise in the uneclipsed WCZ outflow. There is at least one other UV spectrum that shows some C IV λ1550 excess blue emission. It was obtained by *IUE* in 1981 (SWP15072) at orbital phase 0.80. There are unfortunately no UV spectra obtained during that epoch around ϕ=0.36 and no recent UV spectra obtained at other orbital phases.

6. ON THE NATURE OF *Star B*

Early studies of HD 5980 introduced the idea that *Star B* was the WR star in the system. This idea, however, was derived from a noisy RV curve of He II λ 4686 obtained from relatively low resolution photographic spectra. Subsequently, Niemela (1988) obtained RV curves of N IV λ4058 indicating that this line was emitted by *Star B*. Noteworthy is its absence in the 1973-1977 time frame, a time when HD 5980's visual magnitude was at a minimum. The appearance of this line in the early 1980s coincides with a declining *Star A* wind speed. Thus, it appears that the changes in *Star A*'s properties led to changes in the WCZ that allowed N IV λ4058 to become visible in the spectrum, as we already noted in the previous section.

The P Cygni absorption profiles of resonance lines at orbital phases when *Star B* is in front always indicate the presence of very fast outflows ($\geq$3000 km/s) (Koenigsberger et al. 1998a; Georgiev et al. 2011; Hillier et al. 2019). At other orbital phases, the velocities have generally been slower ($\leq$2000 km/s) since the mid-1980s. The very fast wind would be consistent with a WN3/4 or O3 type classification for *Star B*, and the fact that such a fast wind is not observed at phases other than near ϕ=0.36 could be explained by a WCZ that truncates the wind long before terminal speeds are attained. However, it is not easy at this time to discard alternative scenarios. For example, *Star A*'s wind could be non-spherically symmetric such that it is faster in the direction of its companion, or that there is a small population of extremely fast particles produced in the wind-collision process, as found in the hydrodynamic simulations (Pittard 2009) and which would be observable only in the resonance lines.

We currently favor the first scenario because it is simplest and because the N V λ4944 emission clearly splits into two well-defined components during elongations, indicative of orbital motion. This implies an origin in a relatively spherical distribution of gas around *Star B*. However, if the shocked gas can sustain the conditions to produce emission from this N V line, then *Star B* could well be an O-type star rather than a WN, and the very fast wind observed around ϕ=0.36 could be due to one of the other mentioned scenarios.

The radii of the *Star A* and *Star B* occulting disks that were deduced from data of the late 1970s indicate that $R_A > R_B$. Thus, the ϕ=0.36 (*Star B*

in front) eclipse is not total. Hillier et al. (2019) demonstrated that assuming the *Star B* wind can be neglected, the predicted spectrum at ϕ=0.36 is still that of *Star A*, including P Cygni absorptions (see Figures 3 and 4 of Hillier et al. 2019). This provides an explanation for why the spectrum at ϕ=0.36 is, in general terms, so similar to that observed at all other orbital phases, and shows that one cannot adopt the spectrum at this phase as representative of *Star B*'s spectrum. This again opens the possibility that *Star B* may not be a WN star.

It is also interesting to note the high degree of rapid polarimetric variability that was observed around ϕ=0.36 by Villar-Sbaffi et al. (2003). These authors suggested that a very fast rotator model for *Star B* could at least qualitatively explain the observations, although we speculate that a clumpy WCZ might also lead to variable polarization.

Finally, the presence of a second set of photospheric-like absorptions in the 2018 spectrum opens the possibility of an absorption line spectrum associated with *Star B*. The spectrum in question was obtained at orbital phase 0.226 and the second set of absorptions has a velocity of −300 km/s (Figure 19), which however is faster than the expected *Star B* orbital motion at this phase, as deduced from the N Vλ4944 emission. If actually associated with *Star B*'s photosphere, the absorptions would imply that the N Vλ4944 emission arises mainly near the WCZ vertex that is lifted above *Star B*'s surface. However, an alternative explanation is that the blue-shifted absorption lines that mimic photospheric absorptions come from a shell of material surrounding the binary, product of an earlier instability that resulted in the ejection of this material (Barbá et al. 1995).

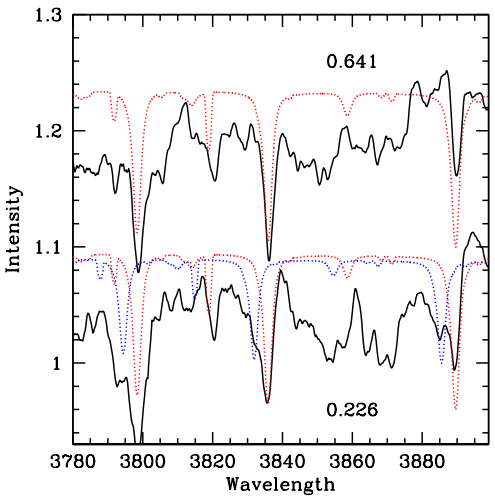

Fig. 19. MagE spectra at orbital phases 0.641 and 0.226 obtained in 2018 showing what appears to be a second set (blue dashes) of photospheric absorption at 0.226 which is shifted by −316 km/s with respect to the absorptions of *Star C* (red dashes). The spectrum at ϕ=0.641 is shifted vertically for clarity in the figure. The wavelength units are Å. The color figure can be viewed online.

7. DISCUSSION AND CONCLUSIONS

7.1. *Summary of Observational Results*

In the previous sections we presented the analysis of high resolution spectroscopic observations obtained since 1998, complemented with historic spectra obtained since the 1950s. The summary of the results is as follows:

1. The integrated emission line intensity in observation epochs 1998-2006 were significantly stronger than in 2009-2016. We define a high state and a low state, corresponding to these two epochs. In the third set of epochs, 2017-2020, the system appears to have been in an intermediate state between low and high.

2. The entire $\lambda\lambda$1200 − 10000 spectral energy distribution had larger intensities during the high state than during the low state.

3. In 1998-1999 and 2017-2020, the integrated emission line intensities vary smoothly over orbital phase with a broad maximum centered around ϕ=0.5-0.6 (apastron). In 2009-2015, the intensities mimic those of 2017-2020 except in the ϕ ≈0.41-0.90 interval, in which they are weaker as a consequence of stronger absorption superposed on the emission, blueward of line center (see Figure 10).

4. The RV curve of N IV λ4058 from data of 1998-2020 is consistent with that of N V λ4944, the latter currently believed to truly represent *Star A*'s orbit. The most significant difference occurs in the phase interval 0.1-0.3 which coincides with maximum approaching velocity of *Star B*. This implies that unresolved N IV *Star B* emission distorts *Star A*'s RV curve. However, the strength of this additional emission changes from epoch to epoch, being stronger during the high state.

5. The Hβ + He II RV curve (data obtained in 1955-2020) display a maximum around the same orbital phase as N IV λ4058, but the peak-to-peak amplitude is a factor of ≈2 smaller. This

implies that there is a significant Hβ + He II contribution arising in *Star B* and the WCZ. This extra emission is mostly evident around the time of periastron during the high state (see Figure 18). The He II λ4686 line behaves similarly to Hβ + He II, but its RVs show significantly more scatter.

6. The phase-dependent FWHM variations in He II λ4686 and H β + He II in all epochs (1955-2020) display a nearly identical descent in the phase interval 0.95-0.05. This phase interval corresponds to the physical eclipse of *Star B* by *Star A*. The available data indicate that the ascent is equally steep. A second minimum in FWHM occurs in the phase interval 0.3-0.6. The descent here appears to be similar in all epochs but the ascent is epoch-dependent (see Figure 7). The most gradual ascent occurred in 1990-2000, when the system was in the high state pre- and post- eruption.

7. The emission line profiles of He II λ5411 in spectra obtained in 2010-2020 in the orbital phase bin $\phi \approx$0.24 are nearly identical (see Figure 10). This is an unexpected result given the strong variability that has characterized HD 5980.

8. The differences between the line profiles of He IIλ5411 observed at ϕ=0.02-0.06 (*Star A* in front) and at ϕ=0.36-0.40 (*Star B* in front) are qualitatively the same in all epochs. In the first of these phases, the line profile is skewed blueward, while in the second of these phases it is skewed redward (see Figure 11). Our recent observations showing this effect (and for which we have spectra at the required orbital phases) were obtained in 1999, 2005, 2010 and 2017. A similar, blueward-skewed profile at $\phi \approx$0.4 was observed also in 1962 (Koenigsberger et al. 2010). The only possible explanation for the blue-shifted emission is the presence of material that flows in the direction of the observer at orbital phases when *Star B* is in front but that, at the same time, is not projected onto either *Star A*'s or *Star B*'s continuum emitting core.

9. Using spectra obtained within the same orbital cycle, we show that the He II line profiles have a strong absorption blueward of line center just before the ϕ=0.36, and that this absorption is replaced by emission just after this phase (see Figure 13 and 14). We attribute this behavior to absorption in the leading WCZ branch as it passes in front of *Star A* just prior to conjunction, and emission from this same region once it is no longer along our line of sight to *Star A*. The velocity range over which the changes occur is approximately −800 to +200 km/s, consistent with the line-of-sight velocities along the wind-collision contact discontinuity that were estimated by Koenigsberger (2004, Figure 20) for the case of a large wind momentum ratio in favor of *Star A*.

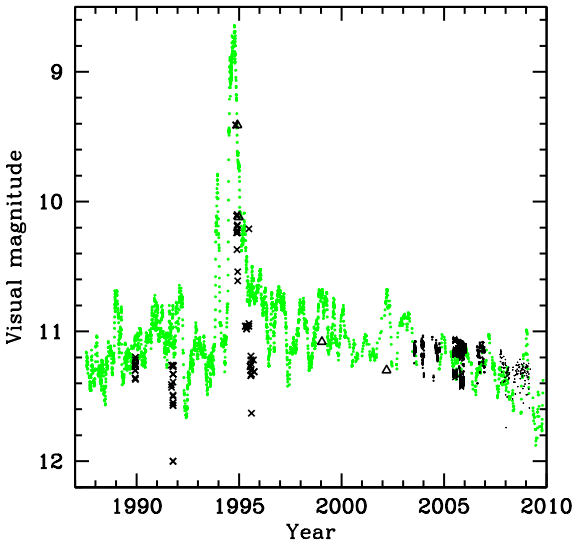

Fig. 20. Historic light curve of HD 5980 in epochs 1987-2010 illustrating the underlying plateau around the time of maximum. Green dots: visual magnitudes obtained by A. Jones shifted by +0.3 mag, after applying a 9-point boxcar average smoothing. Triangles: m_v data listed in Table 6. Black crosses: *International Ultraviolet Explorer* FES magnitudes (Georgiev et al. 2011). Black dots: Swope, SMARTS, ESO, ASAS-SN and LCOGT photometry listed in Table 5. The color figure can be viewed online.

10. A significant amount of hydrogen is evident in the spectra of 1999-2000 and 2014-2016 (Figure 8). In 1999-2000, the lines containing H are stronger at ϕ=0.36 than at ϕ=0.0, 0.15 and 0.83, while in 2014-2016 they are weaker at ϕ=0.36 than at other phases.

7.2. *Star A has Dominated the Emission-Line Spectrum Since 1955*

The evidence leading to this conclusion is the following. First, there has been a persistent presence in all epochs since 1955 of excess blue-shifted emission in He II lines at secondary eclipse (ϕ=0.36). At

this phase, *Star B* is in front and the excess blue emission can only be interpreted as originating in material flowing toward the observer and which lies outside the line of sight to either *Star A* or *Star B*. A wind collision zone that folds around *Star B* and constrains its wind within it is the most feasible scenario to explain the blue-shifted excess. Second, all strong emission lines have displayed RV variations since 1955 that are consistent with their origin in *Star A*. This includes N IV λ4058 which is now strong, but in the past was often absent or too weak to be detected (for example, in 1962-1965, 1973, and 1977). N IV λ4058 became prominent in the 1980s at the same time that the UV lines of Fe V, Fe VI and N IV] λ1486 also emerged. These changes coincided with a reduction in the extent of the UV P Cygni absorptions, indicating a slower wind speed.

The fact that the He II λ4686 and Hβ lines approximately followed the orbit of *Star A* even when N IV λ4058 was weak/absent suggests that the state of *Star A* during the mid-1970s and before was similar to that of a H-rich WN3 star but which intermittently oscillated between WN3 and WN4 before transitioning through the later sub-types as it brightened and headed for the eruption.

Hillier et al. (2019) noted the similarity in the UV P Cyg line profiles that were observed in the early 1980s and early 1990s with those of 2014-2016 (see their Figure 19). Furthermore, Koenigsberger et al. (2010) showed that the line profile variation in He II λ4686 were qualitatively the same in 1962 and 1999 (see their Figures 8 and 9). Specifically, they have a very narrow and blue-shifted shape when *Star B* is in front, compared to elongations, just as is currently observed. Finally, the RV curve of He II λ4686 in the early 1980s displayed a systematic blue-shift precisely around the time of secondary eclipse, indicating that the blue-shifted emission was also prominent in ≈1981-1983 and 1991-1992. This leads to the conclusion that the wind collision region has folded around *Star B* since the 1960s, if not earlier. Thus, *Star A*'s wind has always been the dominant wind in the system.

7.3. *The Emission Line Profile Variations and the Distorted RV Curves are Consistent with a Skewed WCZ that Folds Around Star B and Provides a Source of Excess Emission and Absorption*

The general scenario that emerges is that *Star A*'s wind produces the majority of the emission at line frequencies, and the region where its wind interacts with *Star B* produces a secondary set of emission lines. The strength and location in velocity space of these secondary lines depend on *Star A*'s wind. Thus, the epoch-dependent changes in the WCZ line emission echo the *Star A* wind variations. This explains the varying amplitude of the RV curves obtained at different epochs, the prime example being the N IV λ4058 RV curve. Weak lines that arise from excited transitions are much less affected, as appears to be the case for the He II $\lambda\lambda$6000−6200 lines shown in Figure 18.

We are able to identify the effects caused by the leading WCZ branch when it occults *Star A* at phases just prior to the ϕ=0.36 eclipse and produces absorption superposed on the He II λ5411 emission line. We then see how it produces excess blue-shifted emission shortly thereafter in the same velocity range as observed previously in the absorption. Around the time of the opposite eclipse, the WCZ emission outflow is directed mostly away from the observer, but is largely eclipsed by *Star A*'s opaque disk, and radiation transfer effects through *Star A*'s wind reduce its visibility.

The effects due to the more extended WCZ trailing branch are mostly evident in the photometric eclipse light curves, in the secondary eclipse egress, and in the ϕ ≈0.6 line profiles (see Figure 10).

7.4. *The Brightness Increase Around Periastron*

The *Star A* + *Star B* system is eccentric and the tidal interaction model predicts larger energy dissipation rates around the time of periastron (Moreno et al. 2011). The flux-calibrated HST/STIS spectrum of 1999 at orbital phase 0.15 is ≈5% brighter than at orbital phase 0.83. Table 5 shows that the average visual magnitude is often brighter in the ϕ=0.1-0.2 phase interval, and a brightening at orbital phases after ϕ ≈0.04 was already noted by Sterken & Breysacher (1997).

An alternative interpretation for the continuum brightness increase around periastron is that the wind collision energy is believed to be higher at periastron, which would also lead to a larger brightness at this phase. However, contrary to this expectation, Nazé et al. (2018) found that X-ray maximum occurs close to apastron instead of periastron. This inconsistency between expectations and X-ray observations and the increased brightness around periastron require further investigation.

7.5. *The 1993-1994 Sudden Eruptions*

The long term brightening of the system that started in ≈1980 reached a plateau around the year 2000 where it remained until approximately 2004.

TABLE 5

RECENT PHOTOMETRIC DATA

Epoch Year	JD start -2400000	JD end -2400000	N	ϕ=0.6-0.8 $< m_v >$	s.d.	N	ϕ=0.1-0.2 $< m_v >$	s.d.	Source
2003-04	52838.8	53288.8	33	11.130	0.025	4	11.049	0.010	Swope
2005-07	53561.9	53693.8	138	11.134	0.011	12	11.069	0.006	Foellmi
2005-06	53591.9	54092.7	44	11.132	0.032	36	11.102	0.026	SMARTS
2014/06	56809.9	57080.5	58	11.454	0.028	24	11.433	0.020	ASAS-SN
2015/05	57152.9	57207.8	13	11.409	0.027	5	11.403	0.020	ASAS-SN
2015/07	57222.8	57357.6	19	11.389	0.022	4	11.414	0.052	ASAS-SN
2017/08	57982.7	57985.9	2	11.424	0.008	0	—	—	ASAS-SN
2017/10	58054.5	58073.6	158	11.469	0.029	12	11.472	0.020	LCOGT
2017/11	58074.0	58087.5	190	11.527	0.015	0	—	—	LCOGT
2017-2022	58029.5	59626.5	290	11.37[a]	0.04	109	11.35[a]	0.04	ASAS-SN

[a]These are the average uneclipsed magnitudes obtained in the Sloan g-band between 2017-10-03 and 2022-02-16, and a zero-point shift of +0.14 mag was added to make them consistent with the Johnson V-band magnitudes that were obtained during the same epochs with other instruments.

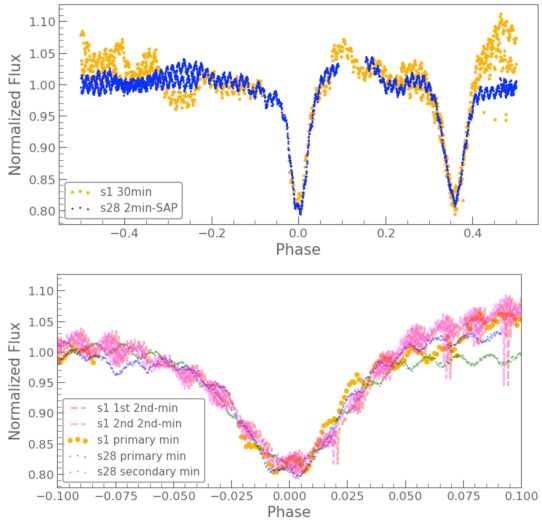

Fig. 21. Normalized TESS photometric data for Sectors 1 and 28 (s1, s28) showing the primary eclipse at phase= 0 and on top of the light curve folded with the period P = 19.2654 d. Clearly seen are the oscillations with a period of $P_{\rm osc}$ = 0.25 d, observed at both eclipses of the *Star A* + *Star B* system. Upper pannel: Two secondary and one primary eclipse were observed in Sector 1 and one primary and one secondary were observed in Sector 28. Lower pannel: As above, but the abscissa gives the distance in orbital phase from mid-eclipse of the five eclipses. The color figure can be viewed online.

Then the brightness and emission line intensities declined reaching an apparent minimum in 2010-2013. The sudden outburst occurred in 1994, with a "precursor" in 1993, both prior to the maximum in the long term trend. We illustrate in Figure 20 the visual magnitude evolution of HD 5980 during the time frame 1987-2010. The complete light curve covering epochs 1950-2018 is presented in Figure 22.

One of the possible scenarios that might explain the long-term behavior is that *Star A* was undergoing an evolutionary transition making it brighter and more extended until it reached a critical radius at which the sudden outburst was triggered. If this were the case, however, it is not clear whether the loss of $\approx 10^{-3}$ $M_\odot$ would have been sufficient to slow the expansion and then allow the star to contract once again to its current state. However, luminous blue variables (LBVs) are known to undergo cyclical changes that impact their photospheric and wind properties. If this were the case, then *Star A* would be the only know LBV with WR spectral spectral characteristics (except possibly the erupting variable in η Carinae).

An alternative interpretation is that the tidal shear energy dissipation in sub-surface *Star A* layers caused it to slowly expand until it reached a critical condition at which an external layer was ejected, thus liberating the accumulated energy. Tidal shear energy dissipation was shown to be a viable mechanism for bloating a star in the case of the red nova V1309 Sco (Koenigsberger & Moreno 2016). In the case of HD 5980, Toledano et al. (2007) outlined the manner in which an increasing stellar radius would lead to increasing tidal shear, eventually causing the eruption.

A more speculative possibility for the outbursts is that they could have been triggered by unstable ac-

cretion of *Star A* material onto *Star B*, as it has been proposed for the case of η Carinae (Soker & Behar 2006). Our observational results leave open the possibility that *Star B* may not be a typical WNE star. The observations indicate that, as *Star A*'s mass-loss rate increased, the WCZ emission also increased, implying a denser collision region. Hydrodynamical wind-wind collision studies show that when the wind momentum of one of the stars is significantly larger than that of its companion, a fraction of the shocked wind is accreted (Matsuda et al. 1992; Ruffert & Arnett 1994; Nagae et al. 2004). Under stationary conditions, the accretion rate is (probably) not sufficient to affect the secondary, but if the incoming stellar wind evolves over time becoming denser and slower, then the numerical simulations find that high density clumps produced by the instabilities in the shocks will fall onto the secondary star (Kashi 2020), potentially leading to non-negligible accretion rates. If such a phenomenon occurred in 1992-1994, the violent expulsion of the material accreted onto *Star B* could have been responsible for the transitory B1.5Ia$^+$ spectrum observed in 1994 and the rapid spectral evolution of the system over the following two years. The persistent underlying WN spectrum at that time (Koenigsberger 2004) would in this case have been that of *Star A*.

7.6. *Future Work*

A treasure trove of information is encoded in the line profile variations. Future investigations could make use of the detailed variability of just a single line such as HeII 5411 to constrain the geometrical extent, general physical conditions, and velocity fields in the WCZ, but to do so requires the use of 3D radiative-hydrodynamic simulations and a densely packed (in orbital phase) set of observations over an entire orbital cycle. Though costly in observing time and computational resources, the expected outcome would include very valuable information on the structure of highly radiative shocks, and would yield a deeper understanding of the *Star A + Star B* interacting system.

Our new RV curves are consistent with those analyzed in Koenigsberger et al. (2014), and thus the derived masses are not expected to change with respect to those obtained previously. Also, the relative continuum luminosities are unaffected by our new results, so the conclusion that both objects are extremely massive and luminous still holds. A possible change lies in what is assumed for the evolutionary state of *Star B*. Its high luminosity suggests a chemically homogeneous evolutionary path (Koenigsberger et al. 2014). However, if it is not a WN star, then a potentially interesting (speculative) scenario is one in which mass transferred from *Star A* to *Star B* via unstable wind accretion has led to sequential violent ejections from *Star B*'s surface reducing its mass and prolonging its main sequence lifetime. Clearly, this conjecture requires the identification of an instability violent enough to eject the material from *Star B*'s surface and leave the system. The alternative conjecture, that *Star A* is the source of the 1993-1994 eruption, also requires further investigation, as no other WNh type star is known to have presented such a violent instability.

The properties of the "third light" source, *Star C* also merit further studies. Although a well-defined photospheric line spectrum is associated with one of the components in this highly eccentric ($e \approx 0.8$, $P_C = 96$ d) system, there is no information as yet regarding the nature of its companion, nor whether it is gravitationally bound to the *Star A + Star B* system. *Star C*'s high eccentricity, line of sight coincidence to the *Star A + Star B* system, and brightness make it tempting to suggest that both binaries may be in a very wide orbit around each other.

Finally, it is also interesting to ponder the question of HD 5980's apparent uniqueness. It may be so only because it is a massive eclipsing system that we have been lucky enough to catch in a very short-lived evolutionary state that many other systems already have or will experience. Given its location in the low-metallicity SMC environment, HD 5980 could be typical of many massive objects yet to be identified in distant extragalactic sources.

This investigation is based on observations obtained at the Las Campanas Observatory, one of the Carnegie Institution for Science Observatories, which we gratefully acknowledge. We thank Abraham Villaseñor for Figure 9. GK thanks the Department of Astronomy at the University of Indiana for hosting a visit during which a large portion of this paper was written, and B. Lazotte for guidance and help in the use of computing facilities. GK acknowledges funding from CONACYT Grant 252499 and UNAM/PAPIIT IN103619. We thank Ricardo Covarrubias and Konstantina Boutsia for obtaining the MIKE observations of 2007 and 2019.

APPENDIX

A. HISTORIC OVERVIEW 1955-2016

Hillier et al. (2019) provided a general historical overview of HD 5980. In this section we incorporate

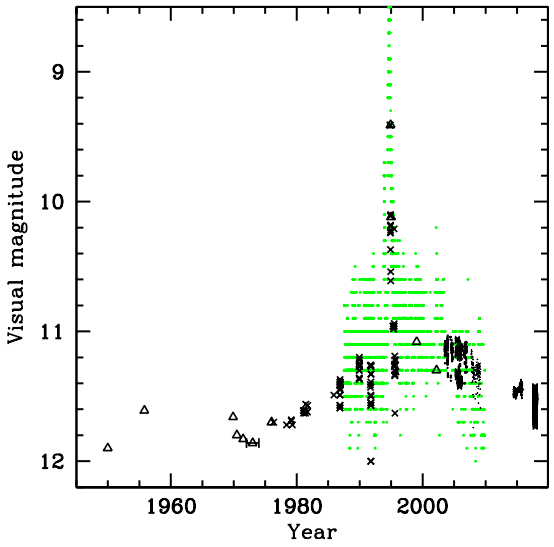

Fig. 22. Same as Figure 20, but here containing all the historic photometric data available. The color figure can be viewed online.

additional information relevant to the problems addressed in this paper.

A.1. *Epoch I: <1981*

The earliest photometric measurements obtained in the early 20th century were summarized by Breysacher (1997). We reproduce these data in Table 6 and in Figure 22. HD 5980 was first observed photometrically by Gascoigne (1954) and subsequently by Feast et al. (1960) who reported it to be variable. Its eclipses were discovered by Hoffmann et al. (1978) and the correct orbital period of 19.3 d determined by Breysacher & Perrier (1980). The photometric light curve described in Breysacher & Perrier (1991) (consisting of 705 Strömgren v filter measurements, obtained in 1979-1981 according to Breysacher (1997)) were analyzed by Perrier et al. (2009), from which the relative continuum emitting radii of *Star A* and *Star B* were deduced, R_A/a=0.158 and R_B/a=0.108, where a is the semimajor axis. The analysis method took into account the presence of an extended semi-transparent envelope around *Star B*, interpreted to be the WR stellar wind, allowing its extent to be estimated, R_{env}/a=0.269. Using the orbital solution of Koenigsberger et al. (2014), who derived $a = 151\,R_\odot$, the relative dimensions were found as $R_A/R_\odot$= 24, $R_B/R_\odot$= 16, $R_{env}/R_\odot$=40.

Koenigsberger et al. (2010) noted the presence of N IV λ4058 in addition to the typical WNE He II λ5411 lines in the spectra of 1955-1962

TABLE 6

HISTORIC VISUAL MAGNITUDES

Epoch	m_v	Reference
1950	11.66	(a)
1955.8	11.61	Feast et al. (1960)
1964-65	11.75	Smith (1968)
1966	11.66	Butler (1972)
1969.9	11.66	Mendoza (1970)
1970-71	11.80	Osmer (1973)
1971-72	11.83	Ardeberg & Maurice (1977)
1972-74	11.86	Azzopardi & Vigneau (1975)
1976	11.7	(d) van den Bergh (1976)
1978-79	11.7	(b) Koenigsberger et al. (2010)
1981	11.6	(b) FES Koenigsberger et al. (2010)
1986	11.4	(b) Moffat et al. (1989)
1989-91	11.25	(b) Koenigsberger et al. (2010)
1994.92	9.41	Barbá et al. (1995)
1994.99	10.12	Koenigsberger et al. (1998b)
1995	11.3:	(b)Koenigsberger et al. (2010)
1999.04	11.08	(e) Massey & Duffy (2001)
2002.2	11.3	(f)

[a]Harvard plates, Barbá Priv.Comm. 2009.
[b]FES magnitudes from IUE.
[c]JD 2440543.604, $\phi \approx$0.26
[d]JD 2443053.76 ($\phi \approx$ 0.55).
[e]Orbital phase unknown.
[f]S. Dufau, Private communication, 2009.

that were obtained at the South African Radcliff observatory, but its absence in a few of the spectra between 1962 and 1965. For example, this line appears to be absent in the spectrum 5581 (1962, ϕ=0.19, Table 11). Walborn (1977) also noted its absence in spectra of 1973 and 1977. These spectra were not published at the time but kindly provided by N. Walborn in the late 1990's and a digitized version[11] is shown in Figure 23. These spectra show strong N IV 3483 but no N IV 4058 above the noise level.

Another interesting feature of spectrum number 5581 is that the He II λ4686 line is clearly blue-shifted with respect to the other spectra. If this shift is real, it would have been one of the few times that a spectral feature associated with *Star B* was seen.

Barbá et al. (1997) also provided an example of a spectrum obtained in 1980 Feb. 2 in which the N IV λ4058 emission line is not evident. In this case, the neighboring H I λ4100 line and other lines, in-

[11]Kindly provided by Orsola De Marco in 1999 who together with Paul Crowther obtained an estimated wavelength calibration.

cluding the N V $\lambda 4603-21$ doublet, are significantly weaker. Two days earlier, on 1980 Jan 31, all these lines were strong and sharp, but significantly narrower than on Feb. 2. This latter spectrum was obtained at $\phi \approx 0.8$, when the lines are generally broader.

Feast et al. (1960) noted the very large variations in the full width at half maximum (FWHM) in He II $\lambda 4686$. These were also seen by Westerlund (1978) who remarked on the sharp minima occurring near the eclipses. The FWHM ranged from 1000 km s^{-1} to 2200 km s^{-1} in spectra of the 1950's. In the few Radcliff spectra with good enough S/N at N IV 4058 and in which this line is visible, it behaved similarly. For example, in spectrum 5212 it had *FWHM*≈500 km s^{-1} while in 3074 it had ≈900 km s^{-1} (Koenigsberger et al. 2010).

Ultraviolet observations by *IUE* obtained in 1978-1981 displayed the P Cygni profiles in the lines of N V 1240, OV 1370, C IV 1550, He II $\lambda 1640$ and N IV 1718 Å typically seen in WNE star. The N V 1240 and C IV 1550 P Cyg absorptions appeared to have two components with the faster one indicating wind speed ≥3000 km s^{-1}(see Figure 2 in Hillier et al. (2019). The semi-forbidden line NIV]1486 was either very weak or absent. In the ≈1800-3200 Å region, no strong emission features were evident.

A.2. *Epoch II: 1981 - 1992*

The first determination of radial velocities as a function of orbital phase was published by Breysacher, Moffat & Niemela (1982 henceforth BMN82), based on data acquired in 1981-1983. These determinations were then complemented with data of 1991-1992 (Moffat et al. 1998). Inspection of the RV curve published in the latter paper shows an apparent maximum around orbital phase 0.1 and an apparent minimum around $\phi \approx 0.3$-0.4. However, the scatter in the data points is too large to say much else.

Niemela (1988) measured the RV variations of the N IV 4058 and N V 4603-21 lines on the same photographic spectra of 1981-1983 discussed in BMN82 and concluded that the NIV line arose mostly from the star which is "behind during primary eclipse". Based on her Figure 1, primary eclipse is at light curve phase $\phi \approx 0$, and the star she concludes is responsible for the N IV emission is approaching at $\phi \approx 0.2$. This would have been *Star B* in our current naming convention.

BMN82 also measured the radial velocities of upper Balmer absorption lines and found a correlation

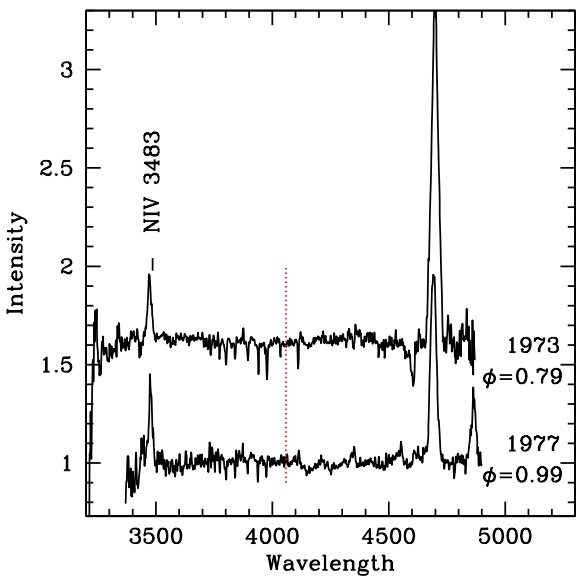

Fig. 23. Spectra obtained by N. Walborn in 1973 and 1977 (unpublished, digitized and calibrated by O. de Marco and P. Crowther). The vertical dotted line indicates the location of the N IV 4058 Å emission line that is notably absent during this epoch. The color figure can be viewed online.

with the upper level of the transition; i.e., optically thicker lines had more negative speeds, and they interpreted this in terms of the lines being formed in an accelerating atmosphere. Given that these lines did not follow the 19.3 d orbit (Niemela 1988), these results must be taken to refer to *Star C*.

Three *IUE* observing campaigns were carried out during this epoch, starting in 1986 with a series of low-resolution spectra covering an orbital cycle (Moffat et al. 1989). These spectra revealed prominent spectral variations that were interpreted in terms of wind eclipses. Specifically, the flux in the NIV 1718 Å emission line and the Fe V-VI pseudo-continuum region become significantly weaker during the phases when *Star B* was in front of *Star A*, compared to the opposite conjunction and to the elongations. The 1989 and 1991 *IUE* campaigns provided a limited number of high resolution spectra over an orbital cycle and showed significantly stronger emission line intensities compared to the spectra that had been obtained in 1979-1981. Particularly relevant was the emergence of strong N IV] 1486 and Fe V/ VI emission lines, all of which displayed RV variations consistent with *Star A*'s orbital motion. The P Cyg absorption components were also less extended, suggesting a slower wind speed. A surprising result was that the slower wind speed was also evident during

elongations, which contradicted the notion that the fast ≈3000 km/s wind arose in *Star B*. The changes prompted the suggestion that HD 5980 was undergoing an outburst (Koenigsberger et al. 1994).

A.3. *Epoch III: 1993-1995*

During this epoch HD 5980 underwent two sudden outbursts superposed on what appears to be a plateau in the average visual magnitude. Both events were observed by Albert Jones, who had been recording visual magnitudes (henceforth, V_J) since the mid 1980's (Bateson & Jones 1994; Bateson et al. 1994). These data[12] showed a "precursor" outburst lasting approximately 90 days (≈JD2449290-2449380 1993 to Oct 29-1994 Jan 27), with a peak brightness V_J ≈9.2. The "base level" before and after this first eruption was V_J ≃10.5. Shortly thereafter, V_J jumped from ≈10.5 on 1994 May 25 to ≈8.2 on 1994 Jul 17 (53 days). The descent started on approximately 1994 Nov 24 and V_J leveled off to ≈10.2 by 1995 August 30.

Koenigsberger et al. (1994) had reported unprecedented changes that were observed in HD 5980's UV spectrum between 1981 and 1992, including a visual magnitude brightening, and suggested that it could be a luminous blue variable (LBV). The spectroscopic discovery of the outburst was reported by Barbá et al. (1994) RV curves of N III 4634-40, N IV 4058 and He II λ5411 constructed with spectra obtained between 1994 December and 1995 August were consistent with the lines originating in *Star A* (Barbá et al. 1996). They classified the 1994 June 18-19 spectrum as WN7.

Photometric monitoring during 1995 November-December by Sterken & Breysacher (1997) yielded an orbital phase-dependent light curve that differed from the one obtained in 1979-1981 (BP91) in that the primary eclipse minimum was much broader and asymmetrical and the secondary eclipse showed more extended "wings". In addition, the light curve had a rounded form between the primary and secondary eclipses, and coherent variability on a timescale of 0.25 d was discovered. These "microvariations" were still detected 24 years later in *TESS* observations (Kołaczek-Szymański et al. 2021).

Monitoring of the outburst with *IUE* started in 1994 November, and the changes in spectral properties between this first UV spectrum and the end of the IUE operations in late 1995 are fully documented in Koenigsberger (2004) and Georgiev et al. (2011). Here we simply note that the IUE spectrum of 1994 November is very similar to that of a B1.5Ia+ star (Koenigsberger et al. 1996) except for the presence of Si IV λ1400 P Cyg features which, however, were interpreted to arise in the "fossil" wind that left the system just prior to the outburst. Because this wind was traveling faster than the outburst ejecta, the "fossil" wind would have been unperturbed by the latter. The maximum speed gleaned from the Si IV P Cyg absorption component is ≈1700 km/s, similar to that derived from an FUV spectrum obtained by ORFEUS on 1993 September 17 (orbital phase 0.075), just ≈42 days prior to the start of the precursor outburst (Koenigsberger et al. 2006). The Si IV P Cyg absorptions are not saturated on the early post-eruption IUE spectra and show substructure that could be interpreted as several pulses having occurred prior to the major outburst.

The reported optical spectra of 1994 September 10-13 (Heydari-Malayeri et al. 1997) are similar to that of the well-known LBV star P Cygni (B1Ia) except for the broad He II λ4686 emission whose strength increased by 50% over a two day time interval. Hillier et al. (2019) remarked on the puzzling presence of this line in these spectra and also in the 1994 December 30 spectrum published in Koenigsberger et al. (1998b), which in addition showed other WNE-type lines (including N IV λ4058). It had been assumed that *Star B* is a H-poor WN star whose wind dominated the spectrum during the late 1970s (Breysacher et al. 1982; Moffat et al. 1998) and that the eruption consisted in a rapid expansion and cooling of the *Star A* outer layers. However, Hillier et al. (2019) noted that according to spectral fits of the *Star A* spectrum, its optically thick wind in 1994 and early 1995 extended out to ≈130-280 $R_\odot$ and would have completely engulfed *Star B*.

The results published by Heydari-Malayeri et al. (1997) include observations of 1993 September 21-23 (a few days after the ORFEUS spectrum mentioned above). These spectra displayed mostly WN6-type lines, although they noted that the relative strength of the N III and He I lines were more typical of WN8.

A.4. *Epoch IV: 1998-2002*

In 1999 HST/STIS observed the system at 5 orbital phases with a sixth phase being obtained in early 2000. A densely spaced set of optical spectra was obtained by FEROS on the ESO 1.5m telescope in 1998-1999 and reported in Schweickhardt et al. (2000) and Kaufer et al. (2002), who analyzed the optical photospheric absorption lines and discovered that the unblended and isolated O III 5592 Å line undergoes RV variations with P≈97 d and suggesting a highly eccentric e ≈0.8 orbit. This result provided

[12] Kindly provided to us during 2002-2008 by A. Jones.

spectroscopic confirmation of the "third light source" in the eclipse light curve solution of Breysacher & Perrier (1981) and later once again confirmed by Perrier et al. (2009).

Koenigsberger et al. (2002) analyzed the HST/STIS spectra of 1999 and showed that the photospheric lines superposed on the Fe V and Fe VI emissions were stationary on the 19.3 d orbital cycle and that they were similar to those of the O3V(f*) star MPG 355, thus providing a strong constraint on the nature of the third light source.

Koenigsberger et al. (2002) obtained an RV curve for the Fe VI 1296 Å emission line based on IUE and HST observations showing a maximum around orbital phase 0.15 and a minimum around 0.5, with a peak-to-peak amplitude ≈270 km/s, confirming that the Fe-lines that first appeared in the mid-1980s still followed the orbital motion of *Star A*.

FUSE observations obtained in 2002 provided FUV continuum and line profiles at 10 orbital phases (Koenigsberger et al. 2006). Most relevant for our current study is that the FUV flux at λ1060 Å in the ORFEUS spectrum that was obtained just prior to the 1993 precursor outburst was very similar to that of the FUSE 2002 spectrum at nearly the same orbital phase. Similarly, the P V 1117 line profiles in both spectra were very similar, except for a small difference in the absorption minimum which in the ORFEUS spectrum reached −1530 km/s and −1760 km/s in the FUSE spectrum. In addition, the line profiles of PV 1117 Å showed wind eclipse effects at orbital phases ϕ=0.92-0.12, indicative of the dense *Star A* wind. The wind-eclipse model led to the conclusion that *Star A*'s accelerating wind was truncated in the direction of the companion.

A.5. *Epoch V: >2003*

A second set of FEROS observations was obtained in 2005-2006. The emission line strength had decreased significantly compared to the set obtained in 1998-1999 (Foellmi et al. 2008). Contemporaneous photometric observations provided a full phase coverage of the secondary eclipse minimum, yielding a minimum m_v ≈11.4. The average value outside eclipses m_v ≈11.1 is listed in Table 5.

Koenigsberger et al. (2014) identified two sets of moving emission lines associated with the N V 4944 Å transition. This transition is significantly less optically thick than the other N V lines visible in the spectrum and is formed very close to the base of the stellar wind. Hence, its radial velocity variations were attributed to orbital motion allowing an estimate of the system's masses (61 ± 10 M$_\odot$, 66 ± 10 M$_\odot$) and orbital separation.

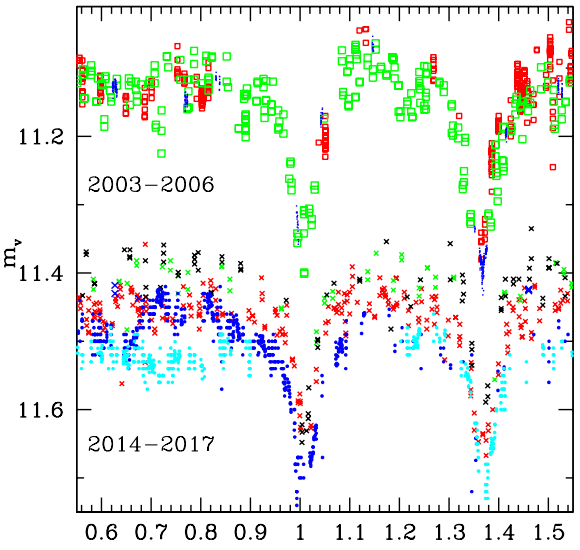

Fig. 24. Photometric light curves for observations obtained in 2003-2006 and in 2014-2017. The abscissa is orbital phase and the ordinate is visual magnitude as determined from the observations with each telescope. No relative shifts have been introduced in this figure. Epochs 2003-2006: SWOPE (red); (Foellmi et al. 2008) (blue), SMARTS (green); Epochs 2014-2017: 2014, ASAS-SN (red), 2015 May, ASAS-SN (green), 2015 July, ASAS-SN (black); 2017 August, ASAS-SN (blue); 2017 Oct, LCOGT (blue dots); 2017 Nov, LCOGT (cyan dots). The color figure can be viewed online.

The more recent data shown in Figure 24 are summarized in Table 5 and consist of ESO Danish photometer data (Foellmi et al. 2008), Swope and SMARTS (Morrell & Massey, unpublished), and ASAS-SN and Las Cumbres Observatory data that were retrieved from the public data bases. Note that the apparent visual magnitudes may not correspond to the same filter system, but they provide a measure of the general brightness at each epoch.

The light curves of this epoch (Figure 24) show a decline by ≈0.35 mag between the years 2003-2006 and 2014-2017. A change in the orbital-phase dependence is also notable: Although both epochs show deep eclipses, the "bump" that is present in the earlier epoch around the time of elongation (ϕ ≈0.6-0.85) seems to have vanished by 2017.

We quantify the average value of the visual magnitude over the phase intervals 0.6-0.8 and 0.1-0.2 in Table 5, showing that $\langle m_v \rangle$ is systematically brighter in the phase interval ϕ=0.1-0.2 in the years 2003-2005 while no significant difference is evident in the

remainder of the epochs listed. Perrier et al. (2009) reported a similar post-periastron brightening.

HST/STIS observations were obtained in 2014 and 2016 and analyzed in Hillier et al. (2019). The most outstanding result concerns the line profile of C IV λ1550 on the two spectra, obtained at eclipse phases. Although the $\lambda\lambda$1200-10000 SED was successfully fit with the CFMGEN model, the observed data showed excess emission shortward of line-center, impossible to account for in the model, in addition to an extent of the P Cyg absorption components far in excess of the wind velocities predicted by the model.

B. LISTS OF OBSERVATIONS

TABLE 7

HIGH DISPERSION LCO SPECTRA

Year	Telescope	Instrument	HJD	Phase
...	...	...	-2400000	19.2654d
2006	DuPont	echelle	53920.861	0.626
2007	Clay Mag 2	MIKE	54342.731	0.524
2008	DuPont	echelle	54670.799	0.553
2008	DuPont	echelle	54671.823	0.606
2008	DuPont	echelle	54672.799	0.656
2008	Clay Mag 2	MIKE	54774.800	0.951
2009	Clay Mag 2	MIKE	55161.687	0.033
2010	Clay Mag 2	MIKE	55205.520	0.308
2010	DuPont	echelle	55341.902	0.387
2010	DuPont	echelle	55342.889	0.439
2010	DuPont	echelle	55480.501	0.581
2010	DuPont	echelle	55481.756	0.646
2010	DuPont	echelle	55482.811	0.702
2010	DuPont	echelle	55506.500	0.931
2010	DuPont	echelle	55507.542	0.985
2010	DuPont	echelle	55508.508	0.035
2010	DuPont	echelle	55509.500	0.087
2010	DuPont	echelle	55510.521	0.140
2010	DuPont	echelle	55511.546	0.193
2010	DuPont	echelle	55512.502	0.243
2011	Clay Mag 2	MIKE	55761.866	0.186
2011	DuPont	echelle	55844.530	0.477
2011	DuPont	echelle	55845.564	0.530
2011	DuPont	echelle	55846.620	0.585

TABLE 7 (CONTINUED)

HIGH DISPERSION LCO SPECTRA

Year	Telescope	Instrument	HJD	Phase
...	...	...	-2400000	19.2654d
2012	Clay Mag 2	MIKE	56084.887	0.953
2012	DuPont	echelle	56120.766	0.815
2013	DuPont	echelle	56496.804	0.334
2013	DuPont	echelle	56497.804	0.385
2013	DuPont	echelle	56498.833	0.440
2013	DuPont	echelle	56501.750	0.592
2013	DuPont	echelle	56502.754	0.643
2013	DuPont	echelle	56533.737	0.252
2015	DuPont	echelle	57154.896	0.493
2015	DuPont	echelle	57157.896	0.649
2017	DuPont	echelle	57766.535	0.242
2017	DuPont	echelle	57767.523	0.293
2017	Magellan II	MIKE	57775.602	0.712
2017	DuPont	echelle	57815.498	0.783
2017	DuPont	echelle	57816.494	0.835
2017	DuPont	echelle	57817.493	0.887
2017	DuPont	echelle	57933.918	0.930
2017	DuPont	echelle	57934.875	0.980
2017	DuPont	echelle	57935.895	0.033
2017	DuPont	echelle	57936.906	0.085
2017	DuPont	echelle	57980.732	0.360
2017	DuPont	echelle	57981.763	0.413
2017	DuPont	echelle	57983.760	0.517
2017	Magellan II	MIKE	57985.895	0.628
2018	Magellan I	MagE	58119.527	0.564
2018	DuPont	echelle	58166.540	0.005
2018	DuPont	echelle	58167.554	0.057
2018	DuPont	echelle	58168.540	0.109
2018	DuPont	echelle	58408.609	0.569
2018	DuPont	echelle	58409.609	0.621
2018	DuPont	echelle	58410.667	0.676
2018	DuPont	echelle	58482.543	0.407
2018	DuPont	echelle	58483.543	0.459
2019	DuPont	echelle	58484.527	0.510
2020	Dupont	echelle	58864.530	0.235
2020	Dupont	echelle	58865.520	0.286
2020	Dupont	echelle	58866.520	0.338

TABLE 8

SUMMARY LOWER DISPERSION LCO SPECTRA

	Telescope	Instrument	Year	HJD -2400000	ϕ_{AB} 19.26d	ϕ_C km/s	V_{Helio}
	Baade Mag 1	IMACS	2009	54900.496	0.476	0.495	+7.06
	Baade Mag 1	IMACS	2009	54902.494	0.579	0.516	+7.41
	DuPont	B&C	2009	55031.832	0.293	0.855	....
	DuPont	B&C	2009	55037.833	0.604	0.917	....
	DuPont	B&C	2009	55038.833	0.656	0.928	....
	Baade Mag 1	IMACS	2009	55072.798	0.419	0.280	-4.78
	Clay Mag 2	MagE	2009	55140.702	0.944	0.983	-12.88
	Clay Mag 2	MagE	2009	55142.508	0.038	0.001	-12.74
	Clay Mag 2	MagE	2009	55143.504	0.089	0.012	-12.74
	Clay Mag 2	MagE	2010	55527.770	0.035	0.991	-12.15
	Baade Mag 1	MagE	2018	58119.527	0.564	0.832	....
	Baade Mag 1	MagE	2018	58436.512	0.018	0.160	-14.3
	Baade Mag 1	MagE	2018	58440.526	0.226	0.201	-14.1
	Baade Mag 1	MagE	2018	58447.511	0.589	0.274	-13.5
	Baade Mag 1	MagE	2018	58448.516	0.641	0.284	-13.4
	Baade Mag 1	MagE	2020	59179.512	0.584	0.906	....

TABLE 9

MATRIX OF ORBITAL PHASES PER EPOCH

Oct 1998	1998-1999	2005	2006-2009	2010-2012	2013	2015	2017	2018	2019-2020
···	0.989	0.982	···	0.985	···	···	0.979	···	···
···	···	0.992	···	···	···	···	···	···	···
···	···	0.007	···	···	···	···	···	0.005	···
···	0.060	0.021	0.033	0.035	···	···	0.033	0.018L	···
···	0.073	···	···	0.087	···	···	0.085	0.057	···
···	0.097	···	···	···	···	···	···	0.109	···
···	···	0.135	···	0.140	···	···	···	···	···
···	0.179	0.163	···	···	···	···	···	···	···
0.204	0.198	···	···	0.193	···	···	···	···	0.235
0.245	0.252	···	···	0.243	0.252	···	0.242	0.226L	···
···	0.268	···	···	···	···	···	0.293	···	0.286
···	0.301	···	···	0.308	0.334	···	0.360	···	0.338
···	···	0.373	···	0.387	0.385	···	···	0.407	···
···	0.405	···	···	···	···	···	0.413	···	···
···	0.436	···	···	0.439	0.440	···	···	···	···
···	0.459	···	···	0.477	···	···	···	0.459	···
···	0.475	···	···	···	···	0.493	0.517	0.510	···
···	0.527	···	0.524	0.531	···	···	···	···	···
···	0.541	···	···	···	0.539	···	···	···	···
0.569	···	···	0.553	···	···	···	···	0.569	···
···	···	···	···	0.582	···	···	···	···	···
···	···	···	0.606	0.586	0.591	···	···	0.589L	···
···	···	···	0.626 ···	···	···	0.628	0.621	···	
···	0.656	···	0.647	···	0.643	0.649	···	0.641L	···
···	0.732	···	···	0.702	···	···	0.712L	0.676	···
···	0.748	0.767	···	···	···	···	···	···	···
···	···	0.800	···	···	···	···	···	···	···
0.827	···	0.815	···	0.815	···	···	0.783	···	···
···	0.838	···	···	···	···	···	0.835	···	···
···	0.887	···	···	···	···	···	0.887	···	···
0.935	0.939	···	···	0.931	···	···	0.930	···	···
0.954	···	0.955	0.953	···	···	···	···	···	···

TABLE 10

N Vλ4944 MEASUREMENTS

HJD	ϕ	RV[1]	RV[2]	RV(NaD)[3]
54670.799	0.553	-78.0	-13.0	-140.0
54671.823	0.606	-126.0	161.0	-140.0
54672.799	0.656	-114.0	165.0	-140.0
54774.800	0.951	-124.0	76.0	-124.0
55140.702	0.944	-55.0	73.0	-127.0
55142.508	0.038	-105.0	130.0	-130.0
55143.504	0.089	-173.0	248.0	-125.0
55143.504	0.089	-174.0	244.0	-127.0
55205.520	0.308	-77.0	134.0	-132.0
55341.897	0.380	-116.0	11.0	-145.0
55342.889	0.439	···	-39.0	-148.0
55480.501	0.581	-101.0	201.0	-127.0
55481.756	0.646	-126.0	206.0	-126.0
55482.811	0.702	-153.0	208.0	-125.0
55506.500	0.931	-73.0	144.0	-125.0
55507.542	0.985	···	41.0	-125.0
55508.508	0.035	13.0	211.0	-125.0
55509.500	0.087	-186.0	245.0	-125.0
55510.521	0.140	-212.0	274.0	-125.0
55511.546	0.193	-216.0	244.0	-125.0
55512.502	0.243	-162.0	230.0	-125.0
55527.770	0.035	-44.0	148.0	-130.0
55761.841	0.185	-178.0	185.0	-142.0
55761.856	0.186	-215.0	214.0	-143.0
55761.874	0.187	-216.0	208.0	-142.0
55761.893	0.191	-206.0	232.0	-142.0
55844.530	0.477	-132.0	42.0	-126.0
55845.564	0.530	-85.0	68.0	-126.0
55846.620	0.585	-113.0	127.0	-126.0
56084.887	0.953	-182.0	-32.0	-147.0
56120.744	0.814	-185.0	150.0	-141.0
56120.765	0.815	-200.0	154.0	-141.0
56120.790	0.817	-195.0	178.0	-141.0
56496.804	0.334	-31.0	127.0	-140.0
56497.804	0.385	-12.0	32.0	-140.0
56498.833	0.440	18.0	41.0	-139.0
56501.750	0.592	-51.0	···	-139.0
56502.754	0.643	-116.0	···	-139.0
56533.737	0.252	-140.0	234.0	-130.0
57154.896	0.493	-100.0	50.0	-149.0
57157.896	0.649	-151.0	···	-150.0
57766.535	0.242	-115.0	229.0	-133.0
57815.498	0.783	-199.0	77.0	-138.0
57817.493	0.873	-102.0	187.0	-138.0
57933.918	0.930	-105.0	150.0	-150.0
57934.875	0.980	···	-23.0	-148.0

TABLE 10 (CONTINUED)

N Vλ4944 MEASUREMENTS

HJD	ϕ	RV[1]	RV[2]	RV(NaD)[3]
57935.893	0.033	-69.0	190.0	-151.0
57936.908	0.085	-180.0	232.0	-158.0
57981.763	0.413	-43.0	52.0	-134.0
57983.760	0.517	-48.0	-6.0	-135.0
57985.895	0.628	-141.0	155.0	-132.0
58166.540	0.005	···	1.0	-138.0
58167.554	0.057	-21.0	226.0	-138.0
58168.540	0.109	-182.0	213.0	-139.0
58408.609	0.569	-157.0	171.0	-124.0
58409.609	0.621	-154.0	220.0	-124.0
58410.667	0.676	-141.0	218.0	-124.0
58440.526	0.226	-142.0	194.0	-124.0
58447.511	0.589	-32.0	176.0	-122.0
58448.516	0.641	-77.0	188.0	-127.0
58482.543	0.407	···	40.0	-128.0
58483.543	0.459	-163.0	35.0	-128.0
58484.527	0.510	-66.0	56.0	-129.0
58864.530	0.235	-151.0	224.0	-133.0
58865.520	0.286	-97.0	184.0	-133.0
58866.520	0.338	24.0	155.0	-134.0
58864.530	0.235	-162.0	213.0	-133.0
58865.520	0.286	-102.0	164.0	-133.0
58866.520	0.338	9.0	176.0	-134.0
55844.530	0.477	-132.0	42.0	-126.0
55845.564	0.530	-85.0	68.0	-126.0
55846.620	0.585	-113.0	127.0	-126.0
56084.887	0.953	-182.0	-32.0	-147.0
56120.744	0.814	-185.0	150.0	-141.0
56120.765	0.815	-200.0	154.0	-141.0
56120.790	0.817	-195.0	178.0	-141.0
56496.804	0.334	-31.0	127.0	-140.0
56497.804	0.385	-12.0	32.0	-140.0
56498.833	0.440	18.0	41.0	-139.0
56501.750	0.592	-51.0	···	-139.0
56502.754	0.643	-116.0	···	-139.0
56533.737	0.252	-140.0	234.0	-130.0
57154.896	0.493	-100.0	50.0	-149.0
57157.896	0.649	-151.0	···	-150.0
57766.535	0.242	-115.0	229.0	-133.0
57815.498	0.783	-199.0	77.0	-138.0
57817.493	0.873	-102.0	187.0	-138.0
57933.918	0.930	-105.0	150.0	-150.0
57934.875	0.980	···	-23.0	-148.0
57935.893	0.033	-69.0	190.0	-151.0
57936.908	0.085	-180.0	232.0	-158.0
57981.763	0.413	-43.0	52.0	-134.0

TABLE 10 (CONTINUED)

N Vλ4944 MEASUREMENTS

HJD	ϕ	RV[1]	RV[2]	RV(NaD)[3]
57983.760	0.517	-48.0	-6.0	-135.0
57985.895	0.628	-141.0	155.0	-132.0
58167.554	0.057	-21.0	226.0	-138.0
58168.540	0.109	-182.0	213.0	-139.0
58408.609	0.569	-157.0	171.0	-124.0
58409.609	0.621	-154.0	220.0	-124.0
58410.667	0.676	-141.0	218.0	-124.0
58440.526	0.226	-142.0	194.0	-124.0
58447.511	0.589	-32.0	176.0	-122.0
58448.516	0.641	-77.0	188.0	-127.0
58482.543	0.407	···	40.0	-128.0
58483.543	0.459	-163.0	35.0	-128.0
58484.527	0.510	-66.0	56.0	-129.0
58864.530	0.235	-151.0	224.0	-133.0
58865.520	0.286	-97.0	184.0	-133.0

TABLE 10 (CONTINUED)

N Vλ4944 MEASUREMENTS

HJD	ϕ	RV[1]	RV[2]	RV(NaD)[3]
58866.520	0.338	24.0	155.0	-134.0
58864.530	0.235	-162.0	213.0	-133.0
58865.520	0.286	-102.0	164.0	-133.0
58866.520	0.338	9.0	176.0	-134.0

Laboratory wavelength used to measure the RVs: N Vλ4944.37, and Na Iλ 5889.9509

[1]Radial velocity of the de-blended component on the left, in units of km s^{-1}, as measured in the observed spectrum and corrected for the SMC velocity. Heliocentric velocity and zero-point shifts in the data by using the NaD measurement listed in Column 5.

[2]Same as in Column 3 but for the de-blended component on the right.

[3]In units of km s^{-1}. This is the centroid of the SMC component of NaD as measured on the observed spectrum.

TABLE 11

COMPENDIUM HE II λ4686 AND Hβ+HE II MEASUREMENTS

Num	Year	HJD	ϕ	RV[1]	FWHM[1]	EW[2]	RV[1]	FWHM[1]	EW[2]	Notes
···	···	-2400000	···	——HeII 4686——			——Hβ+He II——			···
2597	1955	35333.3	0.81	200.	2290.	35.0	128.	1754.	7.7	R
2645	1955	35388.3	0.66	110.	1802.	98.0	16.	1422.	8.7	R
3074	1956	35742.3	0.04	294.	1013.	96.0	396.	973.	11.7	R
3793	1957	···	···	116.	2070.	73.0	265.	1625.	14.0	R
3872	1958	···	···	443.	1217.	79.0	283.	1000.	9.8	R
3882	1958	···	···	258.	1900.	63.0	258.	1000.	8.3	R
4613	1959	36916.3	0.98	181.	1740.	69.0	117.	1740.	18.0	R
4963	1960	···	···	174.	1431.	83.0	74.	1227.	10.7	R
5182	1961	37542.3	0.47	-99.	1095.	107.0	104.	1300.	13.5	R
5212	1961	37572.3	0.03	105.	982.	80.0	280.	1000.	15.3	R
5543	1962	···	···	429.	1973.	54.0	482.	2115.	12.2	R
5571	1962	···	···	388.	1176.	74.0	392.	1249.	14.4	R
5581	1962	37922.3	0.19	-220.	2062.	67.0	-124.	2134.	12.7	R
5586	1962	37925.3	0.35	210.	1517.	68.0	143.	2000.	14.0	R
5594	1962	···	0.60	199.	1511.	71.0	110.	1315.	13.9	R
5601	1962	37933.3	0.77	189.	1858.	69.0	133.	1731.	18.1	R
5602	1962	37946.3	0.44	18.	1300.	77.0	32.	1201.	14.8	R
5603	1962	37954.3	0.86	1730.	1880.	82.0	1410.	2170.	13.2	R
5605	1962	···	0.98	89.	1754.	72.0	230.	1494.	17.5	R
5611	1962	37959.3	0.12	225.	1831.	73.0	363.	1690.	12.4	R
6078	1963	···	···	13.	1713.	67.0	6.	1455.	11.6	R
7127	1965	···	···	200.	2200.	52.0	282.	2390.	11.0	R
···	1973	···	0.79	330::	2300	···	···	69	···	W
···	1977	···	0.99	398::	1927	178::	1541	31	8.8	W
···	1975	42684.6	0.39	···	···	34.3	···	···	4.5	BW
···	1976	42973.6	0.39	···	···	26.5	···	···	2.2	BW
···	1976	43083.6	0.10	···	···	44.0	···	···	5.7	BW
···	1976	43084.6	0.15	···	···	44.5	···	···	6.2	BW
···	1977	43194.6	0.86	···	···	43.6	···	···	7.3	BW
···	81-84	···	···	···	···	82.0	···	···	···	PM
···	1989	47784.4	0.11	···	···	67.0	···	···	···	H-M
···	1991	48618.4	0.39	···	···	87.0	···	···	···	H-M
···	1993	49259.5	0.36	···	···	78.0	···	···	11.8	H-M
···	1994	49605.5	0.73	···	···	1.4	···	···	18.5	H-M
···	1994	49716.8	0.39	156	1400.	81.0	275	900.	41.5	K98
3571	1998	51094.8	0.94	178.	1527.	76.0	243.	1343.	14.3	F
6981	1998	51100.8	0.24	334.	1485.	78.0	322.	1212.	14.1	F
8851	1998	51133.7	0.95	175.	1477.	66.0	146.	1207.	15.6	F
11811	1998	51138.5	0.20	316.	1537.	66.0	291.	1167.	14.9	F
14981	1998	51145.5	0.57	219.	1251.	88.0	152.	1014.	16.4	F
17081	1998	51150.5	0.83	205.	1605.	72.0	151.	1368.	16.1	F
23711	1998	51174.5	0.07	289.	1066.	71.0	252.	920.	15.0	F
24471	1998	51176.5	0.18	309.	1500.	72.0	282.	1197.	14.5	F
25781	1999	51181.5	0.44	154.	927.	67.0	126.	733.	13.0	F
26441	1999	51183.5	0.54	218.	1143.	83.0	154.	909.	16.4	F
27241	1999	51185.5	0.65	239.	1360.	92.0	168.	1158.	17.7	F

TABLE 11 (CONTINUED)

COMPENDIUM He II λ4686 AND Hβ+He II MEASUREMENTS

Num	Year	HJD	ϕ	RV[1]	FWHM[1]	EW[2]	RV[1]	FWHM[1]	EW[2]	Notes
...	...	-2400000	...	——HeII 4686—-			——Hβ+He II ——			...
27941	1999	51187.5	0.75	225.	1565.	86.0	151.	1286.	17.7	F
28681	1999	51189.5	0.85	190.	1617.	68.0	166.	1340.	11.7	F
29441	1999	51191.5	0.95	204.	1564.	64.0	167.	1211.	11.3	F
30311	1999	51193.5	0.06	265.	988.	74.0	229.	851.	15.5	F
31461	1999	51197.5	0.27	315.	1463.	73.0	269.	1021.	15.2	F
1020	1999	51305.3	0.83	367.	1680.	101.0	300.	1500.	25.4	HST
3020	1999	51308.9	0.05	430.	1200.	94.0	390.	1080.	19.0	HST
4020	1999	51310.8	0.15	440.	1560.	103.0	424.	1440.	24.0	HST
5020	1999	51314.9	0.36	357.	1290.	120.0	258.	1135.	20.0	HST
6020	1999	51315.8	0.40	358.	1140.	105.0	296.	1055.	18.0	HST
79411	1999	51375.9	0.53	201.	1173.	102.0	152.	1012.	17.7	F
80871	1999	51379.9	0.73	216.	1554.	111.0	152.	1356.	18.1	F
82121	1999	51381.9	0.84	222.	1552.	96.0	161.	1393.	19.0	F
83811	1999	51383.9	0.94	221.	1497.	93.0	188.	1334.	17.6	F
84511	1999	51384.8	0.99	214.	1382.	105.0	188.	1179.	19.5	F
85181	1999	51385.8	0.04	278.	1080.	91.0	261.	865.	17.0	F
85771	1999	51386.9	0.10	306.	1167.	90.0	299.	1090.	17.8	F
86321	1999	51388.8	0.20	322.	1490.	92.0	341.	1314.	16.7	F
86701	1999	51389.9	0.25	323.	1487.	91.0	338.	1168.	14.9	F
87751	1999	51391.8	0.35	168.	1281.	119.0	136.	1052.	19.6	F
88931	1999	51392.8	0.40	151.	1012.	95.0	105.	953.	18.1	F
90131	1999	51394.9	0.51	180.	1100.	102.0	139.	997.	17.6	F
...	2000	51830.5	0.20	...	...	85.0	...	...	...	MD01
o2020	2000	51655.1	0.01	385.	1320.	94.0	342.	1074.	18.0	HST
617801	2005	53538.9	0.80	217.	1952.	98.0	170.	1792.	17.2	F
620221	2005	53541.9	0.96	251.	1855.	84.0	244.	1590.	13.4	F
710740	2005	53561.9	0.99	239.	1541.	94.0	231.	1215.	15.8	F
725630	2005	53576.8	0.77	269.	1996.	96.0	221.	1803.	15.8	F
925220	2005	53638.7	0.98	235.	1675.	84.0	226.	1346.	13.6	F
928161	2005	53641.7	0.13	340.	1897.	86.0	347.	1716.	14.4	F
1022731	2005	53665.5	0.37	136.	1174.	103.0	95.	1150.	16.7	F
f12	2006	53715.8	0.98	236.	1661.	84.0	224.	1331.	13.7	F
f34	2006	53716.5	0.02	255.	1187.	92.0	214.	928.	14.8	F
f56	2006	53731.5	0.80	218.	1966.	90.0	176.	1858.	15.0	F
f8	2006	53734.6	0.96	245.	1902.	73.0	266.	1561.	13.2	F
f9	2006	53735.5	0.01	243.	1401.	93.0	216.	1160.	16.9	F
f1112	2006	53738.5	0.16	334.	1994.	82.0	298.	1738.	13.0	F
phi476L	2009	54900.4	0.48	135	1442	68	109	1367	10.1	LCO
phi579L	2009	54902.5	0.58	178	1693	71	159	1641	11.3	LCO
phi293L	2009	55031.8	0.29	276	1741	64	247	1601	10.0	LCO
phi604L	2009	55037.8	0.60	257	1784	73	213	1718	11.1	LCO
phi656L	2009	55038.8	0.66	311	1908	73	302	1898	11.8	LCO
phi419L	2009	55072.8	0.42	122.	1237.	58.0	151.	1320.	8.7	LCO
phi944L	2009	55140.7	0.94	273	2011	72	271	1794	11.8	LCO
phi038L	2009	55142.5	0.38	326	1067	61	314	1027	10.6	LCO

TABLE 11 (CONTINUED)

COMPENDIUM He II λ4686 AND Hβ+He II MEASUREMENTS

Num	Year	HJD	ϕ	RV[1]	FWHM[1]	EW[2]	RV[1]	FWHM[1]	EW[2]	Notes
...	...	-2400000	...	——HeII 4686—-			——Hβ+He II ——			...
phi089L	2009	55143.5	0.89	333	1684	63	360	1450	10.5	LCO
phi035L	2010	55527.8	0.04	318	1132	55	317	904	8.0	LCO
o9020	2014	56741	0.0	391	1462	67	356	1239	21.0	HST
phi0.49	2015	57154.9	0.49	97	1371	59	113	1260	10.1	LCO
phi0.65	2015	57157.9	0.65	183	1712	79	106	1507	9.9	LCO
o1140	2016	57653	0.36	259	1415	68	140	1359	23.0	HST
phi564L	2018	58119.5	0.56	182	1434	75	137	1233	12.4	LCO
phi018L	2018	58436.5	0.02	317	1354	76	323	988	12.9	LCO
phi226L	2018	58440.5	0.23	470	1781	62	431	1410	10.5	LCO
phi589L	2018	58447.5	0.59	211	1576	68	136	1391	10.8	LCO
phi641L	2018	58448.5	0.64	228	1658	72	126	1484	10.7	LCO
phi584L	2020	59179.5	0.58	225	1632	69	156	1545	10.5	LCO

Notes: R=Radcliff; BW=Breysacher & West-erlund (1978); H-M=Heydari-Malayeri et al. (1997); K98=Koenigsberger et al. (1998b); F=FEROS; HST=Hubble Space Telescope; MD01= Massey & Duffy (2001); LCO=Las Campanas Observatory; Laboratory wavelength used to measure the radial velocities: λ4685.70 and λ4861.32 from the CMFGEN model spectrum.

[1]In units of km s^{-1}, not corrected for SMC motion.

[2]In units of Å.

[3]The density-to-intensity calibration of this spectrum is uncertain.

TABLE 12

N IVλ3483 AND λ4058

Num	Year	HJD	ϕ	RV[1]	FWHM[1]	EW[2]	RV[1]	FWHM[1]	EW[2]	Notes
...	...	-2400000	...	——N IVλ3483—-			—— N IV λ4058 ——			...
...	1994	49716.8	0.39	bl	bl	1.6	-20	702	0.50	New
3571	1998	51094.8	0.94	...	...	...	3	672	4.1	F
6981	1998	51100.8	0.24	...	...	...	193	505	3.7	F
8851	1998	51133.7	0.95	...	...	...	61	752	4.2	F
11811	1998	51138.5	0.20	...	...	...	231	840	4.8	F
14981	1998	51145.5	0.57	...	...	...	17	744	4.4	F
17081	1998	51150.5	0.83	...	...	...	-22	775	3.9	F
23711	1998	51174.5	0.07	...	...	...	219	786	4.1	F
24471	1998	51176.5	0.18	...	...	...	224	839	4.2	F
25781	1999	51181.5	0.44	...	...	...	60	573	2.4	F
26441	1999	51183.5	0.54	...	...	...	35	639	3.3	F
27241	1999	51185.5	0.65	...	...	...	26	770	3.8	F
27941	1999	51187.5	0.75	...	...	...	281	800	4.1	F
28681	1999	51189.5	0.85	...	...	...	-53	624	2.9:	F
29441	1999	51191.5	0.95	...	...	...	33	578	3.0	F
30311	1999	51193.5	0.06	...	...	...	194	712	5.1	F
31461	1999	51197.5	0.27	...	...	...	142	773	4.3	F
1020	1999	51305.3	0.83	364	1136	5.2	142	1001	4.6	HST
3020	1999	51308.9	0.05	513	1081	3.0	322	926	4.8	HST
4020	1999	51310.8	0.15	422	1300	6.1	378	900	4.0	HST
5020	1999	51314.9	0.36	247	1181	4.9	231	985	4.5	HST

TABLE 12 (CONTINUED)

N IVλ3483 AND λ4058

Num	Year	HJD	ϕ	RV[1]	FWHM[1]	EW[2]	RV[1]	FWHM[1]	EW[2]	Notes
...	...	-2400000	...	——N IVλ3483—-			—— N IV λ4058 ——			...
f8	2006	53734.6	0.96	...	...	...	74	870	3.5	F
f910	2006	53735.5	0.01	...	...	...	145	838	3.1	F
f1112	2006	53738.5	0.16	...	...	...	227	856	2.7	F
phi476L	2009	54900.4	0.48	...	...	...	69	836	1.9	LCO
phi579L	2009	54902.5	0.58	...	...	...	61	966	2.3	LCO
phi293L	2009	55031.8	0.29	...	...	...	151	987	2.2	LCO
phi604L	2009	55037.8	0.60	...	...	...	95	850	2.0	LCO
phi656L	2009	55038.8	0.66	...	...	...	112	952	1.9	LCO
phi419L	2009	55072.8	0.42	...	...	...	124	613	1.7	LCO
phi944L	2009	55140.7	0.94	14	1004	6.1	47	770	2.0	LCO
phi038L	2009	55142.5	0.38	146	1205	6.2	192	896	2.4	LCO
phi089L	2009	55143.5	0.89	161	1163	5.8	236	906	2.4	LCO
phi035L	2010	55527.8	0.04	70	1013	4.2	249	882	1.6	LCO
o9020	2014	56741	0.0	349	1243	5.5	142	941	2.6	HST
phi0.49	2015	57154.9	0.49	...	...	...	22	749	2.0	LCO
phi0.65	2015	57157.9	0.65	...	...	...	-23	825	2.2	LCO
o1140	2016	57653	0.36	236	1273	5.0	144	753	1.9	HST
phi564L	2018	58119.5	0.56	199	1109	4.6:	-21	800	2.8	LCO
phi018L	2018	58436.5	0.02	185	1040	7.8	229	932	3.2	LCO
phi226L	2018	58440.5	0.23	326	997	4.8	257	680	2.5	LCO
phi589L	2018	58447.5	0.59	141	1039	4.6:	35	698	2.4	LCO
phi641L	2018	58448.5	0.64	117	991	4.8	19	711	2.4	LCO
phi584L	2020	59179.5	0.58	90	1117	5.8	59	851	2.0	LCO
f8	2006	53734.6	0.96	...	...	...	74	870	3.5	F
f910	2006	53735.5	0.01	...	...	...	145	838	3.1	F
f1112	2006	53738.5	0.16	...	...	...	227	856	2.7	F
phi476L	2009	54900.4	0.48	...	...	...	69	836	1.9	LCO
phi579L	2009	54902.5	0.58	...	...	...	61	966	2.3	LCO
phi293L	2009	55031.8	0.29	...	...	...	151	987	2.2	LCO
phi604L	2009	55037.8	0.60	...	...	...	95	850	2.0	LCO
phi656L	2009	55038.8	0.66	...	...	...	112	952	1.9	LCO
phi419L	2009	55072.8	0.42	...	...	...	124	613	1.7	LCO
phi944L	2009	55140.7	0.94	14	1004	6.1	47	770	2.0	LCO
phi038L	2009	55142.5	0.38	146	1205	6.2	192	896	2.4	LCO
phi089L	2009	55143.5	0.89	161	1163	5.8	236	906	2.4	LCO
phi035L	2010	55527.8	0.04	70	1013	4.2	249	882	1.6	LCO
o9020	2014	56741	0.0	349	1243	5.5	142	941	2.6	HST
phi0.49	2015	57154.9	0.49	...	...	...	22	749	2.0	LCO
phi0.65	2015	57157.9	0.65	...	...	...	-23	825	2.2	LCO
o1140	2016	57653	0.36	236	1273	5.0	144	753	1.9	HST
phi564L	2018	58119.5	0.56	199	1109	4.6:	-21	800	2.8	LCO
phi018L	2018	58436.5	0.02	185	1040	7.8	229	932	3.2	LCO
phi226L	2018	58440.5	0.23	326	997	4.8	257	680	2.5	LCO
phi589L	2018	58447.5	0.59	141	1039	4.6:	35	698	2.4	LCO
phi641L	2018	58448.5	0.64	117	991	4.8	19	711	2.4	LCO
phi584L	2020	59179.5	0.58	90	1117	5.8	59	851	2.0	LCO

Notes: Same as in Table 11.

N IV reference wavelengths are (3478.7+3483.00+3484.93)/3.=λ3482.21 and λ4057.76.

[1]In units of km s^{-1}, not corrected for SMC motion.

[2]In units of Å.

C. POSSIBLE *Star B* SPECTRUM

In an attempt to extract the *Star B* spectrum, we use the HST/STIS observation obtained in 1999. We shift the ϕ=0.83 and 0.15 spectra in velocity to the *Star A* reference frame (add 180 km/s and subtract 236 km/s, respectively). Then under the assumption that *Star B* is mostly hidden from view at ϕ=0.0, we subtract this eclipse spectrum from the shifted ones. Finally, we shift both residuals in velocity to the rest frame of *Star B*. This is accomplished once again using the RV curve of Koenigsberger et al. (2014). The shifts are, respectively, +320 km/s (ϕ=0.83) and −490 km/s (ϕ=0.15). The result is shown in Figure 25 which suggests that *Star B* emits a relatively narrow (FWHM ∼600 km/s) line at He II λ1640, with no obvious P Cyg absorption. Both N V λ1240 and C IV λ1550 show similarly narrow emission but in this case include an extended P Cyg absorption component extending to −2200 km/s. In the visual range, the He II λ4686 line appears as a relatively weak emission with FWHM∼2300 km/s, as well as many of the other transitions with varying intensities and widths.

The residual spectrum, assumed to correspond to *Star B*, is not the same at both elongations. This is not unexpected given that the emission line profiles differ somewhat between these two phases, as shown in Figure 16. The average continuum flux between 1575-1600 Å is 6.32×10^{-13} (ϕ=0.83) and 7.91×10^{-13} (ϕ=0.15) erg/cm^{2}s in the *Star B* spectrum alone. However, we have already established that the continuum brightness in general is larger around periastron. Because only one *Star A* spectrum was used to obtain the residuals, it is impossible to determine which of the two stars is responsible for the periastron brightening. (The average continuum flux for A+B+C in the ϕ=0.83 and the ϕ=0.15 spectra is, respectively, 3.04×10^{-12}, 3.20×10^{-12}).

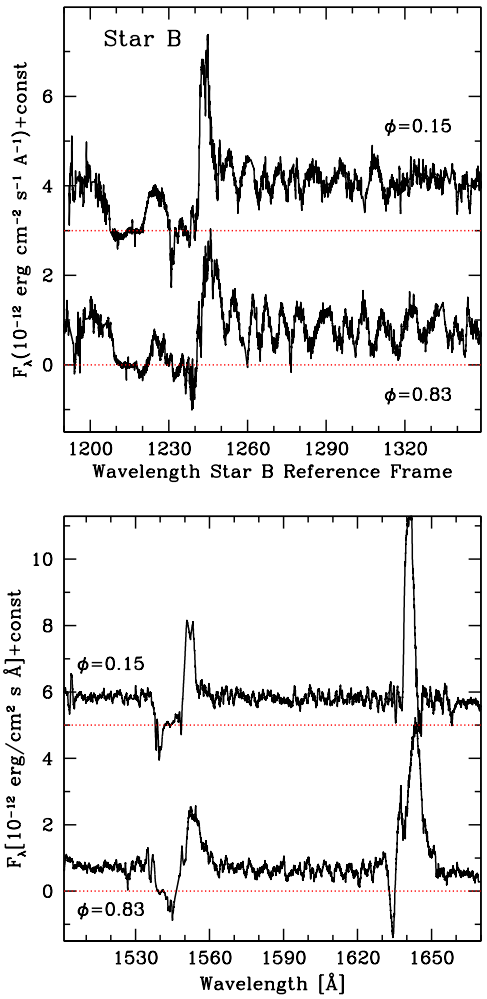

Fig. 25. Difference between the HST/STIS spectrum obtained at elongations in 1999 and the spectrum obtained during primary eclipse (ϕ=0) in 2000. The spectrum at ϕ=0.15 is shifted vertically by $5.\times10^{-12}$ ergs/(s Å). The horizontal dash line indicates the zero flux level. The color figure can be viewed online.

D. EXAMPLE OF THE ECHELLE ORDERS THAT WERE USED TO NORMALIZE ORDER 35

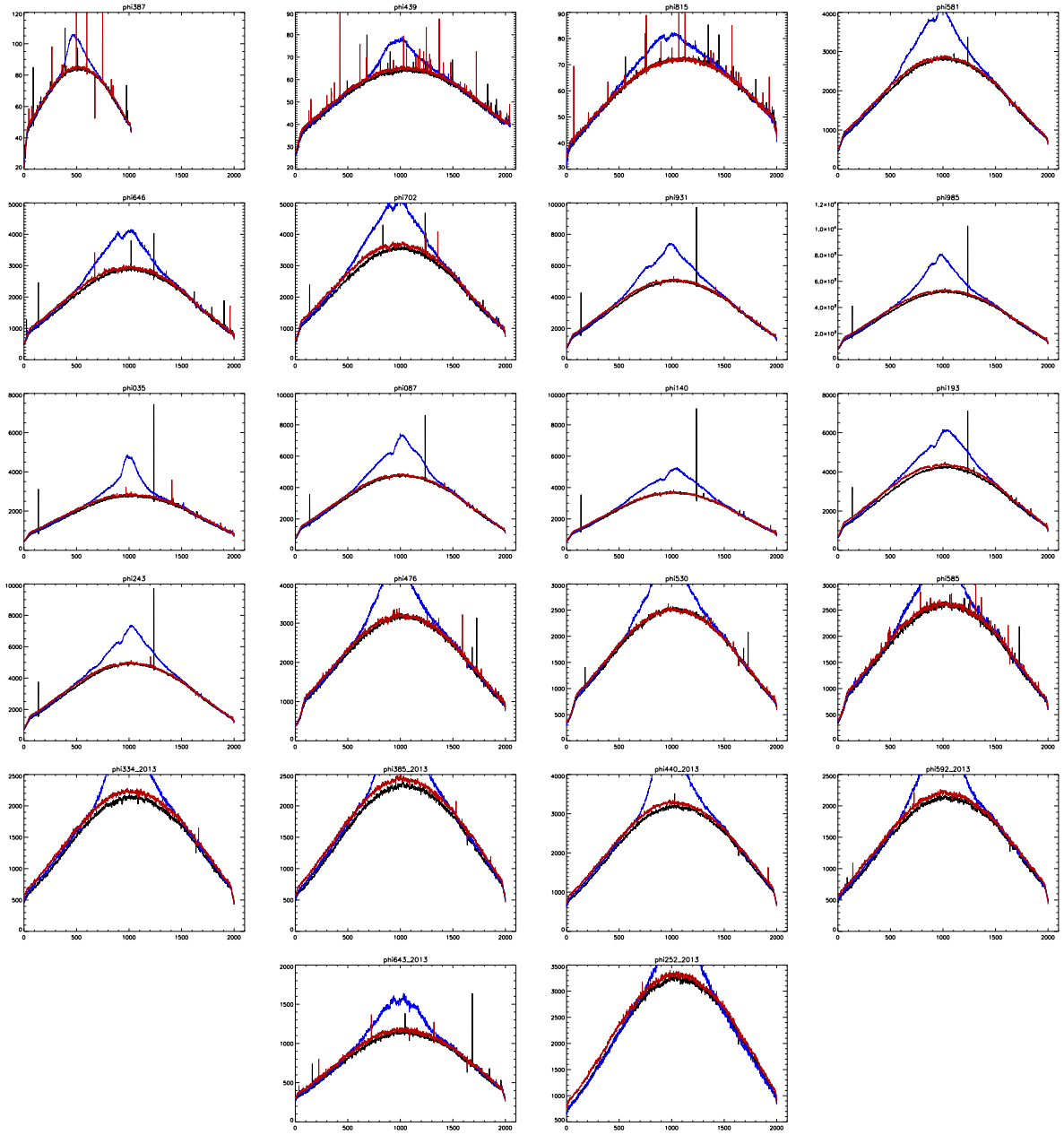

Fig. 26. Echelle orders 34, 36 (red) and 35 (blue), the latter containing the He II λ5411 line. The abscissa shows pixel number on the echelle image. The ordinate shows counts. The normalized profiles were constructed by dividing the counts of order35 by the average counts (order34+order36)/2, after which the spectrum was cleaned of cosmic rays. Each panel is labeled by the orbital phase (2010-2012) and the spectra of 2013 are so labeled. The color figure can be viewed online.

REFERENCES

Ardeberg, A. & Maurice, E. 1977, A&AS, 30, 261

Auer, L. H. & Koenigsberger, G. 1994, ApJ, 436, 859, https://doi.org/10.1086/174963

Azzopardi, M. & Vigneau, J. 1975, A&AS, 19, 271

Barbá, R. H., Morrell, N. I., Niemela, V. S., et al. 1996, RMxAC, 5, 85

Bateson, F. M., Gilmore, A., & Jones, A. F. 1994, IAUC, 6102, 3

Bateson, F. M. & Jones, A. F. 1994, PVSS, 19, 50

Breysacher, J. 1997, ASPC 120, Luminous Blue Variables: Massive Stars in Transition, ed. A. Nota & H. Lamers, 227

Breysacher, J. & François, P. 2000, A&A, 361, 231

Breysacher, J., Moffat, A. F. J., & Niemela, V. S. 1982, ApJ, 257, 116, https://doi.org/10.1086/159969

Breysacher, J. & Perrier, C. 1980, A&A, 90, 207

_____. 1991, IAUS 143, Wolf-Rayet Stars and Interrelations with Other Massive Stars in Galaxies, ed. K. van der Hucht & B. Hidayat (Dordrecht, Kluwer Academic Publisher), 229

Breysacher, J. & Westerlund, B. E. 1978, A&A, 67, 261

Brott, I., Evans, C. J., Hunter, I., et al. 2011, A&A, 530, 116, https://doi.org/10.1051/0004-6361/201016114

Butler, C. J. 1972, DunOP, 1, 133

Cantó, J., Raga, A. C., & Wilkin, F. P. 1996, ApJ, 469, 729, https://doi.org/10.1086/177820

Corcoran, M. F. 2003, IAUS 212, A Massive Star Odyssey: From Main Sequence to Supernova, ed. K. van der Hucht, A. Herrero & E. Céesar (San Francisco, CA: ASP), 130

Ekström, S., Georgy, C., Eggenberger, P., et al. 2012, A&A, 537, 146, https://doi.org/10.1051/0004-6361/201117751

Feast, M. W., Thackeray, A. D., & Wesselink, A. J. 1960, MNRAS, 121, 337, https://doi.org/10.1093/mnras/121.4.337

Foellmi, C., Koenigsberger, G., Georgiev, L., et al. 2008, RMxAA, 44, 3

Foellmi, C., Moffat, A. F. J., & Guerrero, M. A. 2003, MNRAS, 338, 360, https://doi.org/10.1093/j.1365-8711.2003.06052.x

Gayley, K. G. 2009, ApJ, 703, 89, https://doi.org/10.1088/0004-637x/703/1/89

Gayley, K. G., Owocki, S. P., & Cranmer, S. R. 1997, ApJ, 475, 786, https://doi.org/10.1086/303573

Georgiev, L., Koenigsberger, G., Hillier, D. J., et al. 2011, AJ, 142, 191, https://doi.org/10.1088/0004-6256/142/6/191

Heger, A., Langer, N., & Woosley, S. E. 2000, ApJ, 528, 368, https://doi.org/10.1086/308158

Heydari-Malayeri, M., Rauw, G., Esslinger, O., & Beuzit, J.-L. 1997, A&A, 322, 554

Hill, G. M. 2020, Stellar Magnetism: A Workshop in Honour of the Career and Contributions of John D. Landstreet, ed. G. Wade, E. Alecian, D. Bohlender, & A. Sigut, 11, 164

Hill, G. M., Moffat, A. F. J., & St-Louis, N. 2018, MNRAS, 474, 2987, https://doi.org/10.1093/mnras/stx2943

Hill, G. M., Moffat, A. F. J., St-Louis, N., & Bartzakos, P. 2000, MNRAS, 318, 402, https://doi.org/10.1046/j.1365-8711.2000.03705.x

Hillier, D. J., Koenigsberger, G., Nazé, Y., et al. 2019, MNRAS, 486, 725, https://doi.org/10.1093/mnras/stz808

Hillier, D. J. & Lanz, T. 2001, ASPC 247, Spectroscopic Challenges of Photoionized Plasmas, ed. G. Ferland & D. W. Savin (San Francisco, CA: ASPC), 343

Hillier, D. J. & Miller, D. L. 1998, ApJ, 496, 407, https://doi.org/10.1086/305350

Hubeny, I. & Lanz, T. 1995, ApJ, 439, 875, https://doi.org/10.1086/175226

Kashi, A. 2020, MNRAS, 492, 5261, https://doi.org/10.1093/mnras/staa203

Kaufer, A., Schmid, H. M., Schweickhardt, J., & Tubbesing, S. 2002, ASPC 260, Interacting Winds from Massive Stars, ed. A. F. J. Moffat & N. St-Louis (San Francisco, CA: ASPC), 489

Koenigsberger, G. 2004, RMxAA, 40, 107

Koenigsberger, G. & Auer, L. H. 1985, ApJ, 297, 255, https://doi.org/10.1086/163523

Koenigsberger, G., Auer, L. H., Georgiev, L., & Guinan, E. 1998a, ApJ, 496, 934, https://doi.org/10.1086/305398

Koenigsberger, G., Peña, M., Schmutz, W., & Ayala, S. 1998b, ApJ, 499, 889, https://doi.org/10.1086/305659

Koenigsberger, G., Fullerton, A. W., Massa, D., & Auer, L. H. 2006, AJ, 132, 1527, https://doi.org/10.1086/506956

Koenigsberger, G., Georgiev, L., Barbá, R., et al. 2000, ApJ, 542, 428, https://doi.org/10.1086/305529

Koenigsberger, G., Georgiev, L., Hillier, D. J., et al. 2010, AJ, 139, 2600, https://doi.org/10.1088/0004-6256/139/6/2600

Koenigsberger, G., Guinan, E., Auer, L., & Georgiev, L. 1995, ApJ, 452, 107, https://doi.org/10.1086/309719

Koenigsberger, G., Kurucz, R. L., & Georgiev, L. 2002, ApJ, 581, 598, https://doi.org/10.1086/344215

Koenigsberger, G., Moffat, A. F. J., St-Louis, N., et al. 1994, ApJ, 436, 301, https://doi.org/10.1086/174905

Koenigsberger, G., Morrell, N., Hillier, D. J., et al. 2014, AJ, 148, 62, https://doi.org/10.1088/0004-6256/148/4/62

Koenigsberger, G. & Schmutz, W. 2020, A&A, 639, 18, https://doi.org/10.1051/0004-6361/201937305

Koenigsberger, G., Shore, S., Guinan, E., & Auer, L. 1996, RMxAC, 5, 92

Kołaczek-Szymański, P. A., Pigulski, A., Michalska, G., Moździerski, D., & Różański, T. 2021, A&A, 647, 12, https://doi.org/10.1051/0004-6361/202039553

Lamberts, A., Dubus, G., Lesur, G., & Fromang, S. 2012, A&A, 546, 60, https://doi.org/10.1051/0004-6361/201219006
Luehrs, S. 1997, PASP, 109, 504
Maeder, A. & Meynet, G. 2000, ARA&A, 38, 143, https://doi.org/10.1146/annurev.astro.38.1.143
Marchenko, S. V., Moffat, A. F. J., & Koenigsberger, G. 1994, ApJ, 422, 810, https://doi.org/10.1086/173773
Massey, P. & Duffy, A. S. 2001, ApJ, 550, 713, https://doi.org/10.1086/319818
Matsuda, T., Ishii, T., Sekino, N., et al. 1992, MNRAS, 255, 183, https://doi.org/10.1093/mnras/255.2.183
Mendoza, E. E. 1970, BOTT, 5, 269
Moffat, A. F. J., Koenigsberger, G., & Auer, L. H. 1989, ApJ, 344, 734, https://doi.org/10.1086/167838
Moffat, A. F. J., Marchenko, S. V., Bartzakos, P., et al. 1998, ApJ, 497, 896, https://doi.org/10.1086/305475
Moreno, E., Koenigsberger, G., & Harrington, D. M. 2011, A&A, 528, 48, https://doi.org/10.1051/0004-6361/201015874
Münch, G. 1950, ApJ, 112, 266, https://doi.org/10.1086/145341
Nagae, T., Oka, K., Matsuda, T., et al. 2004, A&A, 419, 335, https://doi.org/10.1051/0004-6361:200040070
Nazé, Y., Koenigsberger, G., Pittard, J. M., et al. 2018, ApJ, 853, 164,https://doi.org/10.3847/1538-4357/aaa29c
Nazé, Y. & Rauw, G. 2017, IAUS 239, The Lives and Death-Throes of Massive Stars, 359
Niemela, V. S., Marraco, H. G., & Cabanne, M. L. 1986, PASP, 98, 1133, https://doi.org/10.1086/131910
Osmer, P. S. 1973, ApJ, 181, 327, https://doi.org/10.1086/152051
Paxton, B., Smolec, R., Schwab, J., et al. 2019, ApJS, 243, 10, https://doi.org/10.3847/1538-4365/ab2241
Perrier, C., Breysacher, J., & Rauw, G. 2009, A&A, 503, 963, https://doi.org/10.1051/0004-6361/200911707
Pittard, J. M. 2009, MNRAS, 396, 1743, https://doi.org/10.1111/j.1365-2966.2009.14857.x
Pittard, J. M. & Dawson, B. 2018, MNRAS, 477, 5640, https://doi.org/10.1093/mnras/sty1025
Prilutskii, O. F. & Usov, V. V. 1976, AZh, 53, 6
Puls, J., Urbaneja, M. A., Venero, R., et al. 2005, A&A, 435, 669, https://doi.org/10.1051/0004-6361:20042365
Richardson, N. D., Russell, C. M. P., St-Jean, L., et al. 2017, MNRAS, 471, 2715, https://doi.org/10.1093/mnras/stx1731
Ruffert, M. & Arnett, D. 1994, ApJ, 427, 351, https://doi.org/10.1086/174145
Russell, C. M. P., Corcoran, M. F., Hamaguchi, K., et al. 2016, MNRAS, 458, 2275, https://doi.org/10.1093/mnras/stw339
Schweickhardt, J. 2000, PhD Thesis, Landessternwarte, Heidelberg/Königstuhl
Schweickhardt, J., Wolf, B., Schmid, H. M., et al. 2000, ASPC 204, Thermal and Ionization Aspects of Flows from Hot Stars, ed. H. Lamers & A. Sapar, 113
Shenar, T., Hainich, R., Todt, H., et al. 2016, A&A, 591, 22, https://doi.org/10.1051/0004-6361/201527916
Smith, L. F. 1968, MNRAS, 140, 409, https://doi.org/10.1093/mnras/140.4.409
Soker, N. & Behar, E. 2006, ApJ, 652, 1563, https://doi.org/10.1086/508336
Sterken, C. & Breysacher, J. 1997, A&A, 328, 269
Toledano, O., Koenigsberger, G., & Moreno, E. 2007, ASPC 367, Massive Stars in Interactive Binaries, ed. N. St. -Louis & A. F. J. Moffat, 437
van den Bergh, S. 1976, IAUC 2993, ed. B. G. Marsden, 2
Villar-Sbaffi, A., Moffat, A. F. J., & St-Louis, N. 2003, ApJ, 590, 483, https://doi.org/10.1086/374970

Julia I. Arias and R. Barbá: Departamento de Física, Universidad de La Serena, Av. Juan Cisternas 1200 Norte, La Serena, Chile (jarias@userena.cl).
G. Ferrero and R. Gamen: Facultad de Ciencias Astronómicas y Geofísicas, Universidad Nacional de La Plata, and Instituto de Astrofísica de La Plata (CCT La Plata-CONICET), Paseo del Bosque S/N, B1900FWA, La Plata, Argentina (gferrero@fcaglp.unlp.edu.ar, rgamen@fcaglp.unlp.edu.ar).
D. J. Hillier: Department of Physics and Astronomy, & Pittsburg Particle Physics, Astrophysics and Cosmology Center (PITT PACC), 3941 O'Hara Street, University of Pittsburgh, Pittsburgh, PA 15260, USA (hillier@pitt.edu).
G. Koenigsberger: Instituto de Ciencias Físicas, Universidad Nacional Autónoma de México, Ave. Universidad S/N, Cuernavaca, Morelos, 62210, México (gloria@icf.unam.mx).
N. Morrell: Las Campanas Observatory, Carnegie Observatories, Casilla 601, La Serena, Chile (nmorrell@lco.edu).
W. Schmutz: Physikalisch-Meteorologisches Observatorium Davos and World Radiation Center, Dorfstrasse 33, CH-7260 Davos Dorf, Switzerland (werner.schmutz@pmodwrc.ch).